Complex Langevin approach to interacting Bose gases

Philipp Heinen[1] and Thomas Gasenzer[1,2]

[1]*Kirchhoff-Institut für Physik, Ruprecht-Karls-Universität Heidelberg, Im Neuenheimer Feld 227, 69120 Heidelberg, Germany*
[2]*Institut für Theoretische Physik, Universität Heidelberg, Philosophenweg 16, 69120 Heidelberg, Germany*

Quantitative numerical analyses of interacting dilute Bose-Einstein condensates are most often based on semiclassical approximations. Since the complex-valued field-theoretic action of the Bose gas does not offer itself to the direct application of standard Monte Carlo techniques, simulations beyond their scope by now almost exclusively rely on quantum-mechanical techniques. Here we explore an alternative approach based on a Langevin-type sampling in an extended state space, known as the complex Langevin (CL) algorithm. While the use of the CL technique has a long-standing history in high-energy physics, in particular in the simulation of QCD at finite baryon density, applications to ultracold atoms are still in their infancy. Here we examine the applicability of the CL approach for a one- and two-component, three-dimensional nonrelativistic Bose gas in thermal equilibrium, below and above the Bose-Einstein phase transition. By comparison with analytic descriptions at the Gaussian level, including Bogoliubov and Hartree-Fock theory, we find that the method allows computing reliably and efficiently observables in the regime of experimentally accessible parameters. Close to the transition, quantum corrections lead to a shift of the critical temperature which we reproduce within the numerical range known in the literature. With this work, we aim to provide a first test of CL as a potential out-of-the-box tool for the simulation of experimentally realistic situations, including trapping geometries and multicomponent (or multiple species) models.

I. INTRODUCTION

Interacting Bose-Einstein condensates are at the center of contemporary experimental as well as theoretical studies. Although much of the interest nowadays focuses on nonequilibrium properties, many open questions still remain for Bose gases in equilibrium. A tremendously successful description of the weakly interacting Bose gas is provided by Bogoliubov theory [1]. However, there are many situations of interest where Bogoliubov theory is not very straightforward or even unfeasible to apply. These include Bose gases in trapping potentials [2], in lower dimensions [3], with spin interactions [4], and at phase transitions, to name only a few.

For such scenarios it would be convenient to have a method at hand to simulate the Bose gas from first principles. Unfortunately, the field-theoretic path integral describing the Bose gas in equilibrium may not be simulated by straightforward Monte Carlo methods because the action is complex in general, an obstacle known as the sign problem and that is plaguing numerical computations in a wide range of physical scenarios [5–8].

One possibility to circumvent this problem is to avoid the field-theoretic (coherent state) path integral description of the nonrelativistic Bose gas altogether. This approach is pursued by the path integral Monte Carlo (PIMC) technique [9,10], which treats the problem of interacting bosons in a quantum-mechanical rather that a field-theoretic framework. This method provides exact simulations also for strongly interacting bosons, while its computational cost increases polynomially with the number of particles to be captured.

Other methods stick to the field-theoretic formulation, where there is no limitation on particle number, but employ a semiclassical approximation. These include the truncated Wigner [11,12] as well as the projected Gross–Pitaevskii equation (PGPE) algorithm [13,14].

On the other hand, there are numerical methods available that promise to directly tackle the sign problem in the evaluation of path integrals. These include, *inter alia*, the diagrammatic Monte Carlo method [15,16], the density of states algorithm [17,18], the dual variables approach [18,19], and the fixed node Monte Carlo method [20–22]. Two particularly promising, completely general and model-independent approaches are the Lefschetz thimbles [23,24] as well as the complex Langevin (CL) algorithm [25–27]. Both involve the artificial complexification of real fields, thereby doubling the number of degrees of freedom of the original problem, somewhat similar in spirit to the positive P-representation approach [28–30].

In this work we focus on the complex Langevin algorithm. The method has a long-standing history in the simulation of lattice QCD at finite chemical potential [31–34]. More recently, it has also found applications in condensed-matter physics, mainly in the simulation of nonrelativistic fermions [35,36]. In contrast, works applying CL in the context of bosonic ultracold atoms are scarce, with the notable exception of Refs. [37,38].

063308-1

By performing a systematic study of the three-dimensional interacting Bose gas we here want to demonstrate that CL can also be a useful tool for simulations of ultracold bosonic atoms, in particular because it provides a possibility to perform *exact* simulations within the field-theoretic description of interacting bosons. This paves the way for evaluating observables in equilibrium Bose-Einstein condensates of arbitrary particle number from first principles, without the need of employing any approximation scheme.

II. THE COMPLEX LANGEVIN METHOD

The path integral

$$Z = \int \mathcal{D}\phi \, \exp\left(-S[\phi]\right), \tag{1}$$

for a theory described by the action $S[\phi]$ for the variable or field ϕ, generalizes the partition sum in statistical mechanics and thus offers itself for the numerical evaluation of observables according to

$$\langle \mathcal{O} \rangle_S = Z^{-1} \int \mathcal{D}\phi \, \exp\left(-S[\phi]\right) \mathcal{O}(\phi). \tag{2}$$

In contrast with classical statistical mechanics, where the measure involves a positive-definite probability distribution, the action S in the quantum path integrals (1) and (2) is in general, however, not real-valued. This renders a straightforward Monte Carlo evaluation of the expectation value (2) unfeasible, an obstacle known as the sign problem. Many contributions, by order of magnitude large but positive and negative, can contribute to the sum, both in the real and imaginary parts, to give an eventually comparatively small result. Evaluating this sum generically is exponentially hard [39].

A particular approach developed for tackling this difficulty is the complex Langevin (CL) method [39]. It exploits the well-known equivalence between path integrals and the stochastic Langevin equation as well as the fact that the latter can be formulated also for complex actions. The Langevin approach is well established in statistical mechanics, corresponding to the case of a real-valued action $S[\phi]$ describing, in the simplest case, the dynamics of a real-valued field ϕ. Expectation values of the form (2) can be computed by evolving the field ϕ along a fictitious time ϑ according to the stochastic Langevin equation

$$\frac{\partial \phi}{\partial \vartheta} = -\frac{\delta S}{\delta \phi} + \eta(\vartheta), \tag{3}$$

with $\eta(\vartheta)$ being a Wiener noise averaging to $\langle \eta(\vartheta) \rangle = 0$ and subject to the Markovian covariance $\langle \eta(\vartheta)\eta(\vartheta') \rangle = 2\delta(\vartheta - \vartheta')$, and by taking the average of $\mathcal{O}(\phi(\vartheta))$ along the direction of ϑ. Eq. (3) can be discretized as

$$\phi_{i+1} = \phi_i - \Delta\vartheta \frac{\delta S}{\delta \phi} + \sqrt{2\Delta\vartheta}\,\eta_i, \tag{4}$$

with the η_i being Gaussian random variables with zero mean and standard deviation 1 and $\Delta\vartheta$ being the discretization of the Langevin time.

The CL method extends this scheme for the case of a complex action $S \in \mathbb{C}$. Observing that Eq. (3) leads into the complex plane even for the case of a real-valued field ϕ, one

complexifies each field component, $\phi \to \phi_R + i\phi_I$, which are evolved according to twice as many Langevin equations as before,

$$\frac{\partial \phi_R}{\partial \vartheta} = -\text{Re}\left[\frac{\delta S}{\delta \phi}\right] + \eta_R(\vartheta), \tag{5}$$

$$\frac{\partial \phi_I}{\partial \vartheta} = -\text{Im}\left[\frac{\delta S}{\delta \phi}\right] + \eta_I(\vartheta), \tag{6}$$

with the noise being subject to

$$\langle \eta_R(\vartheta) \rangle = \langle \eta_I(\vartheta) \rangle = 0,$$
$$\langle \eta_R(\vartheta)\eta_R(\vartheta') \rangle = 2N_R\delta(\vartheta - \vartheta'), \quad N_R - N_I = 1, \tag{7}$$
$$\langle \eta_I(\vartheta)\eta_I(\vartheta') \rangle = 2N_I\delta(\vartheta - \vartheta').$$

Hence, the CL equations involve, in general, a stochastic force in both the real and imaginary directions. The two noise contributions must fulfill the condition $N_R - N_I = 1$ in order to ensure that the path integral involves a single integration "direction" as in a line integral [40]. It has been shown, however, that it is numerically most convenient to set $N_R = 1$ and $N_I = 0$ [41].

While it is a straightforward exercise to demonstrate the equivalence of the Langevin approach to the original path integral for real actions, its validity in the case of complex actions cannot be established rigorously. It is known to fail in certain cases, either because of the occurrence of runaway trajectories in the complex plane or because the process converges to an unphysical result [41–43], which both represent characteristic consequences of the sign problem. Several methods have been developed to at least ameliorate the problem of runaways [44–47]. Furthermore, there is substantial numerical evidence that the method can indeed give reliable results in a broad range of physical settings [39]. While the sign problem eventually traces back to the unavoidable complexity of Hilbert space, there have been several attempts to settle the issue by defining criteria for the correctness of the method [41,48–52].

In this paper we rather adopt a hands-on approach and test the complex Langevin approach at the exemplary system of a dilute Bose gas in three dimensions above and below the condensation phase transition. Since the upper critical dimension of the dilute Bose gas is $d_{\text{up}} = 2$, the three-dimensional system is expected to be well-described by mean-field theory close to the phase transition, and thus also further away from it. Hence we evaluate momentum distributions and dispersion relations at different chemical potentials and compare them to analytical predictions from quantum field theory at the mean-field level, using the Bogoliubov and Hartree-Fock approximations below and above the transition, respectively. We moreover explore the more intricate properties near the phase transition and reproduce the shift of the critical temperature within the limits reported in the literature.

In this way we can demonstrate that the CL method represents a promising and easy-to-implement technique for computing many-body observables for interacting bosonic quantum gases in thermal equilibrium. The method can be straightforwardly extended to trapped configurations, multiple components, and more intricate interaction terms, and in principle also lower dimensions where quantum correlations are

expected to play a stronger role and are expected to provide a more stringent test bed of the method.

Since CL is not the only method in the context of ultracold bosonic atoms that employs Langevin-type field equations, some remarks about other stochastic approaches to Bose-Einstein condensates are in order. These mainly include methods based on the positive-P representation, which were already mentioned above, as well as the stochastic Gross–Pitaevskii equation (SGPE) [53–57]. What distinguishes CL from both of them is that it attempts to directly compute the Feynman path integral. The stochastic dynamics thus takes place in a fictitious, unphysical time, during which the Langevin process explores the space of field configurations, i.e., samples from the possible values of the quantum field at each point in space and physical time (the physical time can be either imaginary as in thermal equilibrium or real as in nonequilibrium). In contrast, both the positive-P method and the SGPE are formulated in the physical time of the system, and the stochastic dynamics can be regarded as an actual physical evolution. A further distinctive feature of CL which it shares with the positive-P method but not with the SGPE approach is that it attempts to transform the computationally hard problem of sampling from a nonpositive-definite distribution (as it arises generally when one wants to perform full quantum simulations) to sampling from a positive-definite distribution in a phase space with twice as many degrees of freedom. Thus, for a complex Bose field ψ, both CL and the positive-P method require to evolve *four* real fields instead of two. In contrast, the SGPE does not feature any artificial extension of the number of degrees of freedom. The stochastic term here arises from the coupling of the condensate to the cloud of thermally excited particles. By virtue of including this interaction with the thermal background, the SGPE goes beyond a pure mean-field description, but it does not attempt to solve the full quantum problem from first principles and can rather be classified as a semiclassical method [55]. In this regard it differs from CL and the positive-P approach, which both *in principle* provide exact simulations of the full quantum problem but are not applicable in all situations of interest due to the intrinsic and inevitable complexity of quantum physics.

III. COMPLEX-LANGEVIN SIMULATIONS OF A THERMAL DILUTE BOSE GAS

A. The dilute $\mathcal{N}$-component Bose gas

We study a nonrelativistic $\mathcal{N}$-component Bose gas with U($\mathcal{N}$) symmetric interactions in thermal equilibrium at inverse temperature $\beta = 1/T$ and chemical potential μ.[1] The action, expressed in terms of the complex Bose fields $\psi_a(\tau, \mathbf{x})$, $a = 1, \ldots, \mathcal{N}$, defined on the four-dimensional Euclidean manifold of imaginary time τ and position $\mathbf{x}$, reads

$$S[\psi_a, \psi_a^*] = \int_0^\beta d\tau \int d^3x [\psi_a^* \partial_\tau \psi_a + \mathcal{H}(\psi_a, \psi_a^*)], \quad (8)$$

with Hamiltonian density

$$\mathcal{H}(\psi_a, \psi_a^*) = \frac{1}{2m} \nabla \psi_a^* \cdot \nabla \psi_a - \mu \psi_a^* \psi_a + \frac{g}{2}(\psi_a^* \psi_a)^2, \quad (9)$$

where summation over the field components, $a = 1, \ldots, \mathcal{N}$, is implied, and m is the mass of the particles. For a dilute atomic gas in $d = 3$ dimensions, the dimensionful coupling $g = 4\pi a/m$ is commonly defined in terms of the s-wave scattering length a, while the relevant measure for the coupling strength is the dimensionless gas parameter

$$\eta \equiv \sqrt{\rho a^3}. \quad (10)$$

Being defined in terms of the average density of particles, ρ, it relates a to the mean interparticle spacing $\rho^{-1/3}$ and evaluates, in typical experimental settings, to a number on the order of $\eta \approx 10^{-3}$. Hence, the model is weakly interacting and expected to be well described by low-order perturbative approximations, at least substantially below and above the condensation phase transition.

B. Observables

We are eventually interested in computing correlation functions of operators $\mathcal{O}$ as

$$\langle \mathcal{O}_1 \cdots \mathcal{O}_n \rangle$$
$$= \frac{\int \mathcal{D}\psi_a \mathcal{D}\psi_a^* e^{-S[\psi_a, \psi_a^*]} \mathcal{O}_1(\psi_a, \psi_a^*) \cdots \mathcal{O}_n(\psi_a, \psi_a^*)}{\int \mathcal{D}\psi_a \mathcal{D}\psi_a^* \exp(-S[\psi_a, \psi_a^*])}. \quad (11)$$

Since the action (8) is, in general, not purely real-valued due to the "Berry phase" term $\psi_a^* \partial_\tau \psi_a$, a straightforward Monte Carlo evaluation of the path integral (11) is unfeasible, which thus forms an exemplary problem we plan to tackle using the complex Langevin approach.

In the following, we focus on uniform dilute Bose gases in cubic spatial volumes subject to periodic boundary conditions, such that we can evaluate observables most conveniently in momentum space. The main object we consider is the occupation number of the mode with wave number $\mathbf{k}$,

$$f(\mathbf{k}) = \beta^{-1} \int_0^\beta d\tau \langle \psi_a^*(\mathbf{k}, \tau) \psi_a(\mathbf{k}, \tau) \rangle, \quad (12)$$

where summation over $a = 1, \ldots, \mathcal{N}$ is implied. Exploiting the homogeneity in the τ direction, we average the τ-local expectation value over imaginary time in order to gain a higher statistical accuracy.

Close to the transition and in the condensate phase, f is expected to be much larger than one, $f(\mathbf{k}) \gg 1$, for all modes in the semiclassical regime of momenta below the temperature scale $\mathbf{k}^2/2m \ll T$, where also classical statistical methods such as the truncated Wigner approximation [11,58], or the PGPE algorithm [13] are applicable. At larger momenta, however, where occupancies are small, $f(\mathbf{k}) \ll 1$, the quasiclassical approximation is expected to fail, and one needs either genuine quantum statistical methods or single-particle techniques as the path-integral Monte Carlo (PIMC) algorithm [9]. The PIMC approach is formulated in a quantum-mechanical rather than a quantum field-theoretic framework and thus is limited to comparatively small total

---

[1]Throughout the paper we use natural units where $\hbar = k_B = 1$.

particle numbers. We demonstrate that the CL method is applicable in both the strongly and the weakly occupied regimes.

For the single-component system, $\mathcal{N} = 1$, we additionally extract the dispersion by evaluating

$$\omega(\mathbf{k}) = \beta^{-1} \int_0^\beta d\tau \sqrt{-\frac{\partial_\tau \partial_{\tau'} \langle \psi^*(\mathbf{k}, \tau) \psi(\mathbf{k}, \tau') \rangle|_{\tau'=\tau}}{\langle \psi^*(\mathbf{k}, \tau) \psi(\mathbf{k}, \tau') \rangle|_{\tau'=\tau}}}. \quad (13)$$

The dispersion will give a first measure of the energy of elementary excitations of the system. Also here, exploiting the homogeneity in τ direction, we average $\omega(\mathbf{k})$ over τ in order to gain a higher statistical accuracy.

C. Implementation of the complex Langevin simulations

All our simulations of a one- ($\mathcal{N} = 1$) and a two-component ($\mathcal{N} = 2$) Bose gas were performed on an $N_x N_y N_z N_\tau = 64^3 \times N_\tau$ space-time lattice, with varying discretization $a_\tau = \beta/N_\tau$ along the imaginary-time direction, ranging between $N_\tau = 16$ and $N_\tau = 64$. Details on the discretization of the action (8) and the derivation and form of the corresponding Langevin equations are provided in Appendix A. For simplicity, we fix the temporal units by choosing $(2m)^{-1} = a_s$ in terms of the inverse of the lattice spacing a_s. The temperature and thus β are then given in units of a_s, fixing, for a given N_τ, also the imaginary-time lattice length a_τ in units of a_s. The Langevin time step is set to $\Delta\vartheta = 10^{-3} a_s$.

In each run, we prepared the system in some initial state, as described in the subsequent sections. For example, above the transition, we chose the vacuum state, setting $\psi(\tau, \mathbf{x}) = 0$ at each point on the spatial and temporal lattice. We then propagated the discretized Langevin equations, details of which are provided in Appendix A. After a certain equilibration time that varies with the physical scenario, we can compute averages of the observables along the field trajectories.

The computational cost of a single Langevin time step scales as the total space-time lattice size. In addition to this, also the Langevin evolution time required to reach a fixed statistical precision scales as N_τ, such that the total computational cost scales as $\approx N_x N_y N_z N_\tau^2$. The latter can be inferred from the fact that the action, discretized in τ direction, is of the form

$$S = \sum_{i=1}^{N_\tau} \int d^3x \{\psi_{i+1}^*(\psi_{i+1} - \psi_i) + a_\tau H(\psi_{i+1}^*, \psi_i)\}, \quad (14)$$

where $a_\tau = \beta/N_\tau$ is the imaginary-time step size and H is the discretized Hamiltonian, cf. Appendix A for details. Increasing N_τ for fixed β implies a correspondingly smaller drift term and thus a slower exploration of the space of field configurations, such that a longer Langevin evolution time is required for obtaining the same statistical accuracy.

To speed up the simulation, we parallelized the computation of the Langevin drift and the propagation of the field according to the Langevin equations on GPUs, in a way such that every GPU thread updates a single lattice point. Working on NVIDIA V100 cards, it takes about 40 hours of wall time to evolve a one-component $64^3 \times 16$ lattice for 10^7 time steps and to extract the momentum spectrum after each time step. While for most scenarios we evolved for $\approx 10^7$ steps, we

increased this number to 10^8 steps for the simulations close to the transition in order to gain a higher statistical accuracy needed for the precise determination of the transition point.

Statistical errors are generally estimated from the variance of several independent runs. For further details on the numerical extraction of observables, see Appendix B 1.

D. Ideal gas: Dependence on time discretization

Before we move on to evaluating the observables defined above for an interacting dilute Bose gas at and away from the condensation transition, we perform, as a first benchmark of our approach, CL simulations of an ideal Bose gas. We use this, in particular, to discuss the errors induced by the discretization of imaginary time, corresponding to a truncation of the Fourier representations beyond a highest Matsubara frequency.

For the ideal gas, the coupling vanishes, $g = 0$, and we tune the chemical potential to $\mu = -0.1 a_s^{-1}$, above the phase transition, where the condensate fraction vanishes. We choose the temperature to be $T = 1.25 a_s^{-1}$, which, together with μ corresponds to a total density $\rho = 0.054 a_s^{-3}$ and thus a critical temperature $T_c = [\rho/\zeta(3/2)]^{2/3} 2\pi/m = 0.95 a_s^{-1}$ and a thermal de Broglie wavelength of $\lambda_T = \sqrt{2\pi/mT} = 3.17 a_s$.

We simulate for a Langevin time of $\vartheta_{max} = 10^6 a_s$ and begin the averaging after an equilibration time $\vartheta_0 = 10^5 a_s$. Additionally, we average over 10 independent runs. In each run, we prepare the system in the vacuum state, setting $\psi(\tau, \mathbf{x}) = 0$ at each point on the lattice. The resulting, angular averaged momentum distribution $f_{CL}(k) = f_{CL}(|\mathbf{k}|) = \langle f_{CL}(\mathbf{k}) \rangle_{\Omega_\mathbf{k}}$ for $N_\tau = 16$ is shown in Fig. 1. At large, the results for the distribution agree excellently with the analytic expression,

$$f_{BE}(\mathbf{k}) = \frac{1}{e^{\beta[\varepsilon(\mathbf{k})-\mu]} - 1}, \quad (15)$$

with free single-particle dispersion

$$\varepsilon(\mathbf{k}) = \frac{\mathbf{k}^2}{2m}, \quad (16)$$

over the whole range of momenta, while a weak deviation is seen at the smallest occupancies in the Boltzmann tail. We amplify this discrepancy by showing, in the inset, the relative deviation $(\Delta f/f)_{BE}^{CL} = (f_{CL} - f_{BE})/f_{BE}$ on the same logarithmic momentum scale.

As we recall from Appendix B 3, the occupation number of the ideal gas, on a discrete imaginary-time lattice, can be written as

$$f_{BE}(\mathbf{k}; N_\tau) = \sum_{n=0}^{N_\tau - 1} \frac{1}{N_\tau (e^{2\pi i n/N_\tau} - 1) + \beta[\varepsilon(\mathbf{k}) - \mu]}. \quad (17)$$

We show the relative deviation $(\Delta f/f)_{BE}^{N_\tau} = [f_{BE}(\mathbf{k}) - f_{BE}(\mathbf{k}; N_\tau)]/f_{BE}(\mathbf{k})$ as a dotted line in the inset of Fig. 1, which agrees on average with the deviation $(\Delta f/f)_{BE}^{CL}$ between the CL data and the exact result. This, in particular, demonstrates that the systematic increase of the relative numerical error in the low-occupancy region at large momenta can be attributed to the truncation of the Matsubara series.

To further corroborate this observation, we have performed runs with a different number of lattice points N_τ
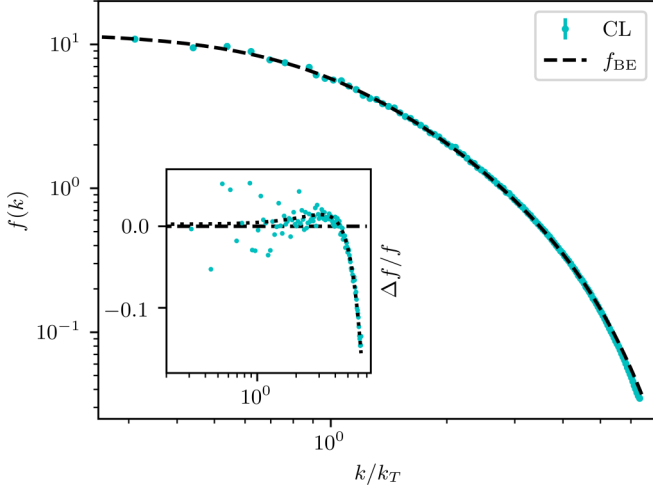
FIG. 1. Angle-averaged momentum spectrum $f_{CL}(k)$ of a single-component, noninteracting gas above the Bose-Einstein phase transition, at a temperature $T = 1.25a_s^{-1}$ and chemical potential $\mu = -0.1a_s^{-1}$ (in units of the lattice constant a_s), as obtained by means of the complex Langevin method on a $64^3 \times N_\tau$ lattice, with $N_\tau = 16$ imaginary-time points. The momentum is measured in units of the inverse thermal de Broglie wavelength $k_T = \lambda_T^{-1} = \sqrt{mT/2\pi} = 0.315a_s^{-1}$. The black dashed line represents the Bose-Einstein distribution $f_{BE}(k)$. The inset shows the relative deviation $(\Delta f/f)_{BE}^{CL} = (f_{CL} - f_{BE})/f_{BE}$ of the numerical and continuum analytic distributions. Note that the statistical error is generally higher for smaller k because the corresponding momentum shells contain less modes to average over. The dotted black line in the inset represents the relative deviation as predicted from the analytical finite-N_τ computation. Note that here (and in all plots above the transition) for better visibility the spectrum is shown only up to $k_{max} = 2a_s^{-1}$, i.e., excluding the "corners" of the momentum lattice. A version including the corners, i.e., up to $k_{max} = 2\sqrt{3}a_s^{-1}$, is shown in Fig. 15, Appendix B.

along the imaginary-time direction. The respective deviations $(\Delta f/f)_{BE}^{CL}$ and $(\Delta f/f)_{BE}^{N_\tau}$ for $N_\tau = 16, 24, 32$ are compared with each other in Fig. 2. As one can see, the deviation of the CL data from the exact Bose-Einstein distributions decreases with increasing N_τ, as predicted by the analytical finite-N_τ results shown as dashed lines.

The dispersion of the ideal Bose gas, $\omega_{CL}(k) = \omega_{CL}(|\mathbf{k}|) = \langle \omega_{CL}(\mathbf{k}) \rangle_{\Omega_\mathbf{k}}$, obtained as an angular average over (13), is shown for $N_\tau = 16$ in Fig. 3. The continuum dispersion is given by the basic free-gas kinetic energy, shifted by the chemical potential,

$$\omega_{BE}(\mathbf{k}) = \varepsilon(\mathbf{k}) - \mu, \tag{18}$$

while the finite-size dispersions result, as described in Appendix B 3, as

$$\omega_{BE}(\mathbf{k}; N_\tau)$$

$$= \sqrt{\frac{-N_\tau^2 T^2}{f(\mathbf{k}; N_\tau)} \sum_{n=0}^{N_\tau - 1} \frac{2e^{-2\pi i n/N_\tau} - e^{-4\pi i n/N_\tau} - 1}{N_\tau(e^{2\pi i n/N_\tau} - 1) + \beta[\varepsilon(\mathbf{k}) - \mu]}}. \tag{19}$$

The deviation between the CL and continuum analytic results is visibly larger, but can be attributed, as for the momentum
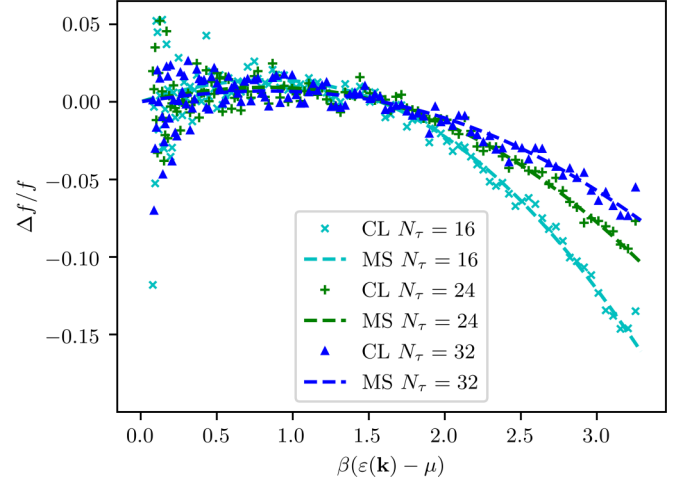

FIG. 2. Comparison between the relative deviation $(\Delta f/f)_{BE}^{CL} = (f_{CL} - f_{BE})/f_{BE}$ of the numerical and analytic, (15), Bose-Einstein distributions (CL, points) and the finite-size deviation $(\Delta f/f)_{BE}^{N_\tau} = [f_{BE}(\mathbf{k}; N_\tau) - f_{BE}(\mathbf{k})]/f_{BE}(\mathbf{k})$ due to the truncation of the Matsubara series (MS, dashed lines), as a function of $\beta(\varepsilon(\mathbf{k}) - \mu)$. The data are obtained for the same parameters as in Fig. 1, but for three different $N_\tau \in \{16, 24, 32\}$.

spectrum f, to the finite lattice resolution in imaginary-time direction and thus to the corresponding truncation of the sum over the Matsubara frequencies. This is again corroborated by a comparison of the deviation for different N_τ, as shown in Fig. 4.
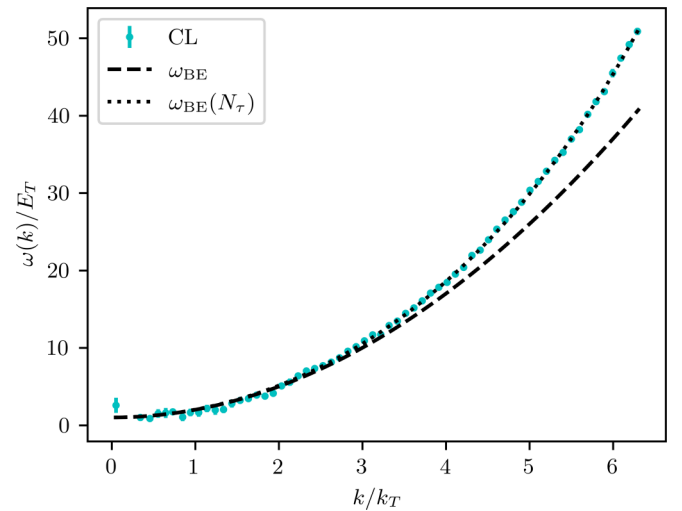

FIG. 3. Dispersion $\omega_{CL}(k)$ of the ideal Bose gas, as obtained according to Eq. (13) from the same data as used in Fig. 1 and averaged over the angular orientations of $\mathbf{k}$, in units of $E_T \equiv k_T^2/2m$. Note that, for better visibility, we doubled the width of the momentum bins in comparison to Fig. 1. The black dashed line indicates the free-gas dispersion (18), whereas the corresponding prediction (19) on a discrete temporal lattice is shown as a dotted black line. The momentum is measured in units of the inverse thermal de Broglie wavelength $k_T = 0.315a_s^{-1}$.
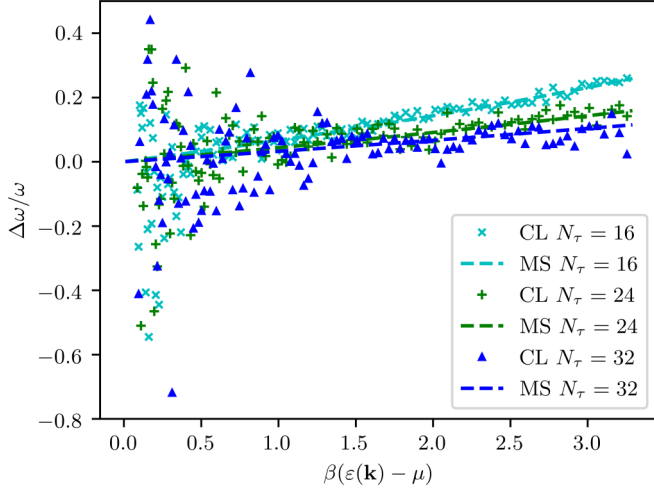
FIG. 4. Comparison between the relative deviation $(\Delta\omega/\omega)^{CL}_{BE} = (\omega_{CL} - \omega_{BE})/\omega_{BE}$ of the numerical and analytic, (18), free gas dispersion and the finite-size deviation $(\Delta\omega/\omega)^{N_\tau}_{BE} = [\omega_{BE}(\mathbf{k}; N_\tau) - \omega_{BE}(\mathbf{k})]/\omega_{BE}(\mathbf{k})$ due to the truncation of the Matsubara series, as a function of $\beta[\varepsilon(\mathbf{k}) - \mu]$. The data are obtained for the same parameters as in Fig. 1, but for three different $N_\tau \in \{16, 24, 32\}$.

E. Interacting gas above the Bose-Einstein condensate phase transition

Having performed first benchmark computations for an ideal Bose gas, we now turn to a weakly interacting, i.e., dilute gas and use the complex Langevin approach to calculate momentum spectra and dispersions for chemical potentials and temperatures away from and near the condensation phase transition. We start with considering the case above the transition, where we can compare our numerical results to analytic predictions on the basis of the Hartree-Fock (HF) Gaussian approximation. Subsequently, we benchmark our CL results to Bogoliubov theory below the transition, for both one- and two-component systems. Finally, we explore the vicinity of the phase transition, where we can obtain a benchmark beyond mean-field theory by computing the relative shift of the critical temperature due to interactions, a quantity that is sensitive to non-Gaussian fluctuations. Above the critical point, we use the CL approach to compute the observables for the same choice of temperature and chemical potential, but with a nonvanishing, positive coupling constant $g = 1a_s^2$, quantifying the repulsive contact interactions between the bosons. Our simulations return, for the chosen parameters, a density of $\rho = (0.0447 \pm 0.002)a_s^{-3}$, where we have extracted ρ as described in Appendix B. The corresponding diluteness parameter η, Eq. (10), is found to be $\eta \approx 1.7 \times 10^{-3}$, which is within the range typically reached in cold-gas experiments. Note, that, with the basic implementation of the method as described here, in the grand-canonical ensemble formulation, we can freely choose temperature and chemical potential, while the mean energy and density are obtained from the numerical data. This procedure can be straightforwardly extended to systematically determine the Lagrange parameters from given mean thermodynamic quantities.

Figure 5 shows the momentum spectrum of the dilute gas in analogy to the ideal-gas spectrum depicted in Fig. 1, on a
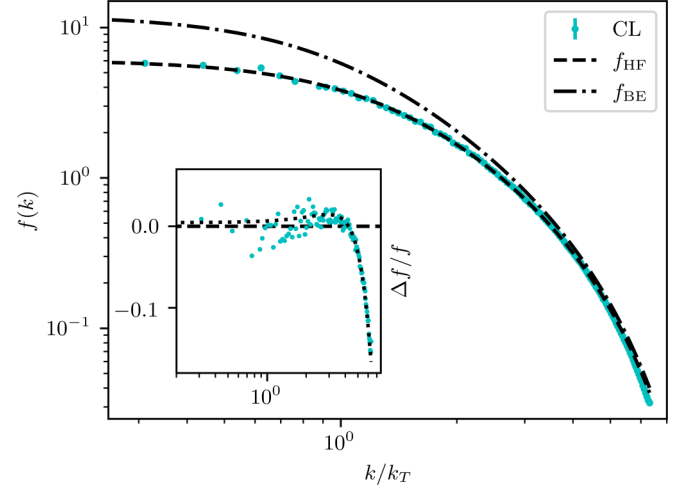

FIG. 5. Angle-averaged momentum spectrum $f_{CL}(k)$ of an interacting single-component gas above the BEC phase transition. Temperature and chemical potential are chosen as in Fig. 1, the coupling strength is $g = 1.0a_s^2$, giving rise to a diluteness $\eta \approx 1.7 \times 10^{-3}$. The momentum is measured in units of the inverse thermal de Broglie wavelength $k_T = \lambda_T^{-1} = \sqrt{mT/2\pi} = 0.315a_s^{-1}$. The CL data are shown on a $64^3 \times N_\tau$ lattice, with $N_\tau = 16$ and averaged over 10 runs. The spectrum fits well with the one calculated within the Hartree-Fock approximation (dashed black line). For comparison we include the Bose-Einstein distribution of the corresponding noninteracting system (dash-dotted black line). The inset shows the relative deviation $(\Delta f/f)^{CL}_{HF} = [f_{CL}(k) - f_{HF}(k)]/f_{HF}(k)$. The dotted black line in the inset represents the deviation $(\Delta f/f)^{N_\tau}_{HF} = [f_{HF}(k; N_\tau) - f_{HF}(k)]/f_{HF}(k)$ of the finite-N_τ from the $N_\tau \to \infty$ version of the HF spectrum.

$64^3 \times N_\tau$ lattice, with $N_\tau = 16$. The main panels demonstrates good agreement with results obtained within the Hartree-Fock (HF) approximation [59], as described in the following.

Expanding the Hamiltonian (9) in leading order of a mean-field approximation corresponds to replacing the quartic term by

$$(\psi^*\psi)^2 \to 4\langle\psi^*\psi\rangle\psi^*\psi + (\langle\psi^*\psi^*\rangle\psi\psi + \text{c.c.}). \quad (20)$$

Above the transition, we can neglect the in general complex anomalous densities $\langle\psi\psi\rangle$ such that the resulting Hamiltonian describes, again, a noninteracting Bose gas, albeit with a shifted chemical potential

$$\mu' = \mu - 2g\langle\psi^*\psi\rangle. \quad (21)$$

The mean particle density $\rho = \langle|\psi|^2\rangle$, which equals the momentum integral over the Bose-Einstein distribution, hence must be determined self-consistently; that is, by solving the equation

$$\rho = \int \frac{d^3k}{(2\pi)^3} f_{BE}(\mathbf{k}; \mu') = \lambda_T^{-3} g_{3/2}(e^{\beta(\mu-2g\rho)}). \quad (22)$$

To determine ρ and from this μ', we numerically solve Eq. (22), evaluating the polylogarithm directly. We obtain $\rho_{HF} = 0.0454a_s^{-3}$ which can be compared with the density obtained from our CL simulations as indicated above. The density corresponds to $\mu' = -0.191a_s^{-1}$, which gives the ideal-gas Bose-Einstein distribution $f_{HF}(k)$ shown as the

dashed line in Fig. 5, which significantly deviates from the dash-dotted distribution f_{BE} for μ.

The inset of Fig. 5 shows the relative deviation $(\Delta f / f)^{\mathrm{CL}}_{\mathrm{HF}} = [f_{\mathrm{CL}}(k) - f_{\mathrm{HF}}(k)]/f_{\mathrm{HF}}(k)$ from the expected Hartree-Fock result and compares it to the deviation $(\Delta f / f)^{N_\tau}_{\mathrm{HF}} = [f_{\mathrm{HF}}(k; N_\tau) - f_{\mathrm{HF}}(k)]/f_{\mathrm{HF}}(k)$ of the finite-N_τ from the $N_\tau \to \infty$ version of the HF spectrum, on a temporal lattice of $N_\tau = 16$ points. This demonstrates good agreement over the whole range of momenta.

F. Bose gas in the condensed phase

Before we move on to studying the region close to the BE phase transition, we repeat the previous analysis away from criticality, in the condensed phase. In a condensate, the pattern of possible collective excitations fundamentally changes due to spontaneous symmetry breaking. While the Hugenholtz-Pines (or Goldstone) theorem implies the elementary excitations to be gapless in the zero-energy limit, the interactions suppress density vs phase fluctuations, such that long-range phase coherence prevails which renders the long-wavelength excitations sound like. In the case $\mathcal{N} > 1$ of more than one internal component of the U($\mathcal{N}$) symmetric model (9), however, additional Goldstone excitations are possible, which correspond to relative density variations between the components. These excitations are not subject to the suppression by interactions, which depend on the total density $\sum_{a=1}^{\mathcal{N}} \psi_a^* \psi_a$ only and are therefore similar to the motion of noninteracting bosons. To explore our algorithm for this case, too, we consider, in the following, systems with both $\mathcal{N} = 1$ and $\mathcal{N} = 2$.

1. One-component system

We start again with the single-component system, $\mathcal{N} = 1$, for which we now choose a temperature $T = 0.625a_{\mathrm{s}}^{-1}$, chemical potential $\mu = 0.5a_{\mathrm{s}}^{-1}$, and coupling constant $g = 0.1a_{\mathrm{s}}^2$. This results in a total density of $\rho \approx \mu/g = 5a_{\mathrm{s}}^{-3}$, corresponding to a diluteness $\eta = 0.56 \times 10^{-3}$. As before, we work on a $64^3 \times N_\tau$ lattice, with different choices of the imaginary-time size $N_\tau = 16$.

It turns out, though, that initializing the field as $\psi(\tau, \mathbf{x}; \vartheta = 0) = 0$ for the Langevin evolution, as we did for all runs above the phase transition, the Langevin process is not able to build up a condensate, i.e., a highly over-occupied $\mathbf{k} = 0$ mode even at temperatures far below the transition, at least not within the limited simulation time available. This could be expected for large systems as the relative size of the phase space covered by the condensate mode is inversely proportional to the system size.

When starting instead from a spatially uniform, nonvanishing field configuration given by the semiclassical mean-field value $\psi(\tau, \mathbf{x}) \equiv \sqrt{\mu/g}$, the CL process leads to only a slight modification, which consists in a thermal depletion of the condensate mode and the buildup of the corresponding distribution of momentum excitations shown in Fig. 6.

From Bogoliubov mean-field theory one expects the momentum distribution of the single-component gas to be [1]

$$f_{\mathrm{Bog}}(\mathbf{k}) = \frac{1 + 2v_{\mathbf{k}}^2}{e^{\beta\omega_{\mathrm{Bog}}(\mathbf{k})} - 1} + v_{\mathbf{k}}^2, \qquad (23)$$
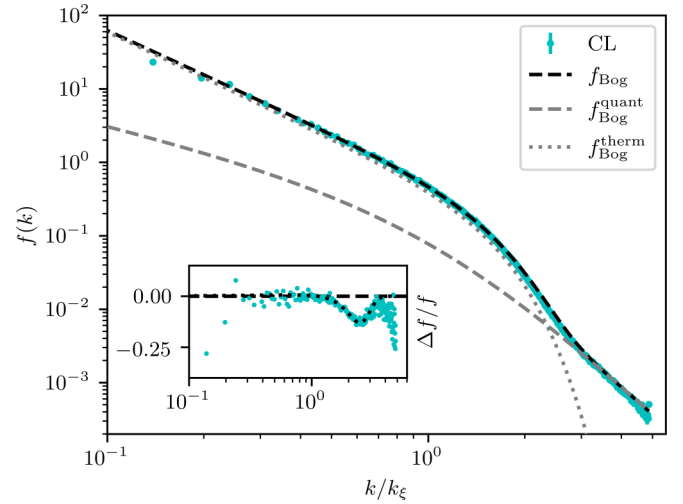

FIG. 6. Momentum spectrum of the interacting single-component gas below the phase transition, at temperature $T = 0.625a_{\mathrm{s}}^{-1}$, chemical potential $\mu = 0.5a_{\mathrm{s}}^{-1}$, and for a coupling $g = 0.1a_{\mathrm{s}}^2$, corresponding to a diluteness $\eta \approx 0.56 \times 10^{-3}$. It is obtained from CL dynamics on a $64^3 \times (N_\tau = 32)$ lattice, averaged over four runs starting from a state with constant density $\rho_0 = \mu/g = 5a_{\mathrm{s}}^{-3}$. The CL process leads to a slightly larger condensate density $\rho_0 = f(0)/\mathcal{V} = (5.0309 \pm 0.0002)a_{\mathrm{s}}^{-3}$, corresponding to $f(0) \approx 1.32 \times 10^6$, while the condensate depletion becomes $\rho' \equiv \rho - \rho_0 = (0.0149 \pm 0.0001)a_{\mathrm{s}}^{-3}$. Momenta are given in units of the healing momentum $k_\xi = \sqrt{2mg\rho_0} = 0.71a_{\mathrm{s}}^{-1}$. The dashed black line represents the spectrum (23) predicted by Bogoliubov theory, consisting of a thermal (dotted gray line) and a quantum depletion (dashed gray line) part. The inset shows the relative deviation $(\Delta f / f)^{\mathrm{CL}}_{\mathrm{Bog}} = (f_{\mathrm{CL}} - f_{\mathrm{Bog}})/f_{\mathrm{Bog}}$ of the CL data from the Bogoliubov spectrum. The dotted black line indicates an estimate of the deviation $(\Delta f / f)^{N_\tau}_{\mathrm{Bog}} = [f_{\mathrm{Bog}}(k; N_\tau) - f_{\mathrm{Bog}}(k)]/f_{\mathrm{Bog}}(k)$ of the finite-N_τ from the $N_\tau \to \infty$ version of the Bogoliubov spectrum, cf. the main text.

where

$$v_{\mathbf{k}} = \sqrt{\frac{1}{2}\left[\frac{\varepsilon(\mathbf{k}) + g\rho_0}{\omega_{\mathrm{Bog}}(\mathbf{k})} - 1\right]}, \qquad (24)$$

in which ρ_0 denotes the condensate density

$$\rho_0 = \rho - \mathcal{V}^{-1}\sum_{\mathbf{k}\neq 0} f_{\mathrm{Bog}}(\mathbf{k}), \qquad (25)$$

with spatial volume $\mathcal{V}$. The Bogoliubov dispersion of the elementary excitations is given in terms of the free dispersion $\varepsilon(\mathbf{k})$, Eq. (18), by

$$\omega_{\mathrm{Bog}}(\mathbf{k}) = \sqrt{\varepsilon(\mathbf{k})[\varepsilon(\mathbf{k}) + 2g\rho_0]}. \qquad (26)$$

Note that the quasiparticle dispersion is soundlike, $\omega_{\mathrm{Bog}}(\mathbf{k}) \simeq c_{\mathrm{s}}|\mathbf{k}|$, at momenta below the healing-length scale $k_\xi = \sqrt{2mg\rho_0}$.

The second contribution to (23), $v_{\mathbf{k}}^2$, gives rise to the quantum depletion, i.e., it accounts for all particles that are not in the condensate mode due to the interactions even at $T = 0$. The first term, which is proportional to the thermal occupancy of the quasiparticles, approximated as being noninteracting,
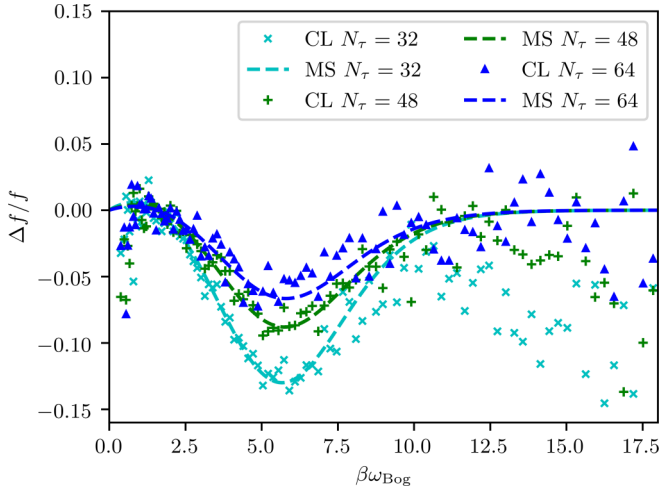
FIG. 7. Comparison between the relative deviation $(\Delta f/f)_{\mathrm{Bog}}^{\mathrm{CL}} = (f_{\mathrm{CL}} - f_{\mathrm{Bog}})/f_{\mathrm{Bog}}$ of the numerical and Bogoliubov, (23), distributions (CL, points) and the finite-size deviation $(\Delta f/f)_{\mathrm{Bog}}^{N_\tau} = [f_{\mathrm{Bog}}(k; N_\tau) - f_{\mathrm{Bog}}(k)]/f_{\mathrm{Bog}}(k)$ due to the truncation of the Matsubara series (MS, dashed lines), as a function of $\beta\omega_{\mathrm{Bog}}$. The data are obtained for the same parameters as in Fig. 6, but for three different $N_\tau \in \{32, 48, 64\}$. Note that for better visibility we doubled the width of the momentum bins in comparison with Fig. 6.

accounts for the fraction of particles, which are noncondensed due to thermal excitations.

In Fig. 6, we show the spectrum (23) as a black dashed line, which hardly deviates from our numerical data, as reflected by the relative deviation $(\Delta f/f)_{\mathrm{Bog}}^{\mathrm{CL}} = (f_{\mathrm{CL}} - f_{\mathrm{Bog}})/f_{\mathrm{Bog}}$ depicted in the inset. The gray dotted and dashed lines indicate the contributions to the analytic spectrum (23), which account for the thermal and quantum depletion of the condensate, respectively.

We estimate the deviation caused by a finite N_τ by replacing the thermal distribution of noninteracting quasiparticles in Eq. (23) by the finite-N_τ expression, as we did this for the ideal gas,

$$\frac{1}{e^{\beta\omega_{\mathrm{Bog}}(\mathbf{k})} - 1} \to \sum_{n=0}^{N_\tau - 1} \frac{1}{N_\tau(e^{2\pi i n/N_\tau} - 1) + \beta\omega_{\mathrm{Bog}}(\mathbf{k})}. \quad (27)$$

As can be inferred from the inset of Fig. 6, this captures the residual deviation between the CL and Bogoliubov distributions up to momenta above which the quantum depletion becomes more relevant than the thermal one.

In Fig. 7 we compare the deviations of the distributions obtained with CL and the Bogoliubov distribution with the respective deviations of the finite-N_τ estimate from the full Bogoliubov distribution, for three different $N_\tau \in \{32, 48, 64\}$. This demonstrates that the Matsubara series truncation also affects the region of high momenta where v_k^2 dominates the spectrum.

Also the Bogoliubov dispersion, which we show in Fig. 8, is well reproduced by the CL simulations.

Finally, it is important to note that the CL method is not only able to describe the part of the momentum spectrum which is dominated by thermal excitations but also to reproduce the occupation numbers at high momenta where
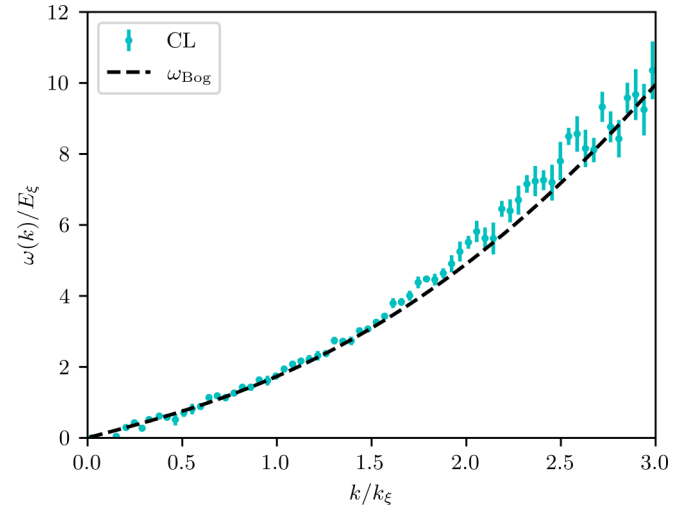

FIG. 8. Dispersion of the interacting single-component gas below the phase transition in units of $E_\xi \equiv k_\xi^2/2m$, as obtained according to Eq. (13) from the same data as used in Fig. 6 and averaged over the angular orientations of $\mathbf{k}$. Note that for better visibility we doubled the width of the momentum bins in comparison to Fig. 6. For comparison we show the dispersion predicted by Bogoliubov theory as a black dashed line.

the spectrum is dominated by the quantum contribution. To further corroborate this observation, we also performed a simulation for a much smaller temperature, $T = 0.15625 a_s^{-1}$, i.e., we increased N_τ to 128. For such low temperatures, the spectrum is almost entirely dominated by the quantum depletion. Still, the spectrum is accurately reproduced by CL, see Fig. 9. This gives hope that CL is a suitable tool for performing exact simulations also in the quantum regime.
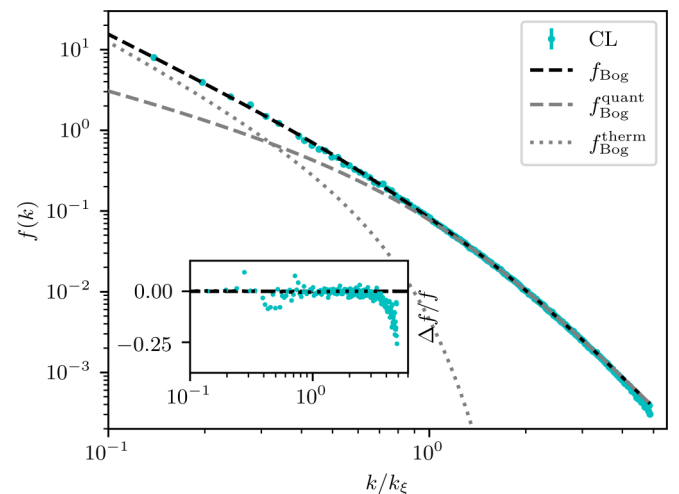

FIG. 9. The same as in Fig. 6, but for $T = 0.15625 a_s^{-1}$ and $N_\tau = 128$. At this low temperature, large parts of the spectrum are dominated by the quantum depletion, yet CL is still able to precisely describe the spectrum.
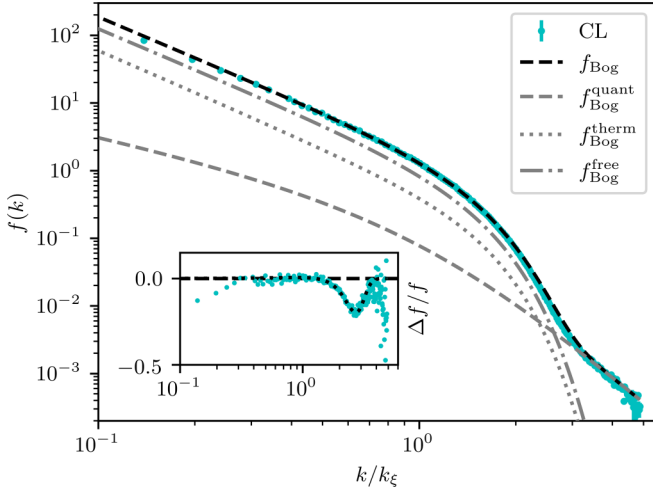
FIG. 10. Momentum spectrum of the interacting two-component gas below the phase transition. The system is described by the U(2)-symmetric Hamiltonian (9), i.e., $\mathcal{N} = 2$. Parameters are, as before, $T = 0.625a_s^{-1}$, $\mu = 0.5a_s^{-1}$, and $g = 0.1a_s^2$, $N_\tau = 32$, averaging over three runs. The spectrum (28) predicted by $\mathcal{N}$-component Bogoliubov theory is represented by the black dashed line. For comparison, we have also plotted the quantum (dashed gray line) and thermal (dotted gray line) contributions, as well as the contribution from the free Goldstone relative number excitations between the two internal components (dashed-dotted line). The inset shows the relative deviation $(\Delta f/f)_{\mathrm{Bog,tot}}^{\mathrm{CL}} = (f_{\mathrm{CL}} - f_{\mathrm{Bog,tot}})/f_{\mathrm{Bog,tot}}$ of the CL data from the Bogoliubov spectrum. The dotted black line shows an estimate of the deviation $(\Delta f/f)_{\mathrm{Bog,tot}}^{N_\tau} = [f_{\mathrm{Bog,tot}}(k; N_\tau) - f_{\mathrm{Bog,tot}}(k)]/f_{\mathrm{Bog,tot}}(k)$ of the finite-N_τ from the $N_\tau \to \infty$ version of the Bogoliubov spectrum, cf. the main text.

2. Two-component system

We have repeated the above simulations for the case of a two-component system, with U(2) symmetric Hamiltonian (9). From Bogoliubov theory [see Appendix C for a summary for the general U($\mathcal{N}$) case], one obtains, as mentioned initially, besides the gapless elementary excitations of the total density with dispersion (25), an additional free Goldstone mode with dispersion given by (18) for each of the remaining $\mathcal{N} - 1$ degrees of freedom. For the case of general $\mathcal{N}$, the total momentum distribution reads

$$
\begin{aligned}
f_{\mathrm{Bog,tot}}(\mathbf{k}) &= \sum_{a=1}^{\mathcal{N}} \langle |\psi_a(\mathbf{k})|^2 \rangle \\
&= \frac{1 + 2v_{\mathbf{k},\mathcal{N}}^2}{e^{\beta\omega_{\mathrm{Bog}}(\mathbf{k})} - 1} + v_{\mathbf{k},\mathcal{N}}^2 + \frac{\mathcal{N} - 1}{e^{\beta\varepsilon(\mathbf{k})} - 1},
\end{aligned} \quad (28)
$$

where

$$
v_{\mathbf{k},\mathcal{N}} = \sqrt{\frac{1}{2}\left[\frac{\varepsilon(\mathbf{k}) + \mathcal{N}g\rho_0}{\omega_{\mathrm{Bog}}(\mathbf{k})} - 1\right]}, \quad (29)
$$

We show the results of our CL simulations in Fig. 10 and compare them to the total Bogoliubov distribution (28), as well as to the quantum and thermal contributions from the Bogoliubov and free modes, respectively.

G. Interacting system at the transition

We finally would like to explore the CL approach to the dilute Bose gas close to the Bose-Einstein phase transition. We start by considering the occupation number spectrum to show a pure Rayleigh-Jeans power law in the IR as a signature of the phase transition, before we move on to determining the shift of the critical temperature due to interactions in the real Bose gas.

1. Rayleigh-Jeans scaling

At the transition, we expect the occupation number to show Rayleigh-Jeans scaling,

$$
f(\mathbf{k}) \sim \frac{1}{|\mathbf{k}|^2}, \quad (30)
$$

for small $|\mathbf{k}|$ in the infinite-volume limit. In principle, this could provide a method for determining the transition point, which, in practice, however, is suited only for obtaining a rough estimate of where the phase transition occurs. On the one hand, statistical errors are in general large for the relevant small momentum modes; on the other hand, in finite-size systems, even at the transition, Rayleigh-Jeans scaling is not expected to be realized down to vanishing momenta.

As reported in the previous section, the formation of a condensate by the Langevin process can take unrealistically long computation times. Hence, for simulations below the transition, a condensate must be seeded by choosing a non-vanishing zero-mode population in the initial configuration for the Langevin process. However, since we do not know *a priori* at which chemical potential condensation occurs, it is most convenient to approach the critical point from the noncondensed phase. Nonetheless, the fact that the Langevin equilibration time strongly increases for a condensed state gives us a further (numerical) indication for determining the transition point.

We choose a temperature $T = 1.25a_s^{-1}$ and a coupling $g = 0.5a_s^2$, resulting in a density $\rho \approx 0.08a_s^{-3}$ and thus a diluteness of $\eta \approx 0.8 \times 10^{-3}$. From HF theory, one obtains the transition to occur at $\mu = 2g\rho_c^0$, with ρ_c^0 the critical density in the free system. This amounts to $\mu_c^{\mathrm{HF}}/T = 0.066$ for chosen temperature and coupling. We perform simulations for five values of the chemical potential between $\mu/T = 0.056$ and $\mu/T = 0.063$. The Langevin time evolution of the accumulated average of the zero-mode occupancy,

$$
f(0) \equiv \langle f(0, \vartheta) \rangle_{\vartheta_0}^{\vartheta_{\max}} = \frac{1}{\vartheta_{\max} - \vartheta_0} \int_{\vartheta_0}^{\vartheta_{\max}} d\vartheta\, f(k = 0, \vartheta), \quad (31)
$$

is shown in Fig. 11, as a function of the maximum Langevin time $\vartheta_{\max}$ and for $\vartheta_0 = 2.5 \times 10^3 a_s$. While we observe a fast convergence in $\vartheta_{\max}$ for $\mu/T = 0.056$ and 0.06, i.e., still rather far away from the transition, the convergence of $f(0)$ appears to be more and more slowed down for $\mu/T = 0.062$, 0.0625, and 0.063, especially for the latter value of the chemical potential, giving a first hint that the system approaches the transition. To make sure that our results are reliable and not biased by insufficient simulation time, we performed additional runs with a nonzero seed of $\psi = 0.075a_s^{-3/2}$, corresponding to $f(0) \approx 1475$, for the case of the largest chemical potential,
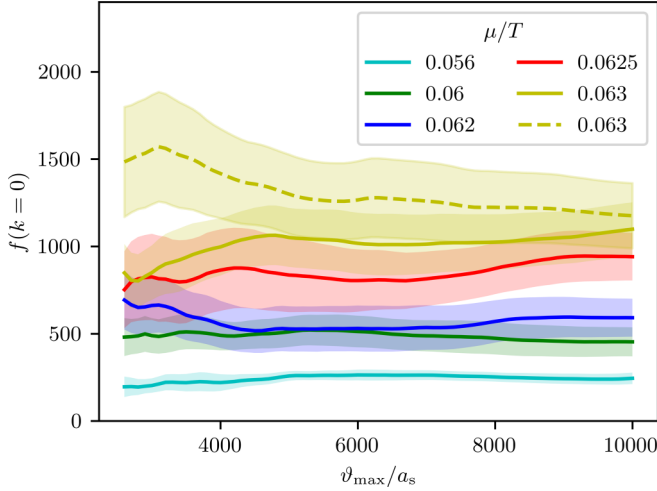
FIG. 11. Langevin evolution of the zero mode occupancy $f(0)$ averaged over Langevin times $\vartheta = \vartheta_0, \ldots, \vartheta_{\max}$, cf. (31), as a function of $\vartheta_{\max}$, with $\vartheta_0 = 2.5 \times 10^3 a_s$, for five different chemical potentials μ close to the transition, with chemical potential decreasing from the uppermost to the lowermost curve, at a temperature $T = 1.25 a_s^{-1}$, coupling $g = 0.5 a_s^2$. The data are obtained on a $64^3 \times (N_\tau = 16)$ lattice and the resulting densities $\rho \approx 0.08 a_s^{-3}$ correspond to a diluteness $\eta \approx 0.8 \times 10^{-3}$. For $\mu/T = 0.056, 0.06, 0.062, 0.0625$, no seed of the zero mode was given. For $\mu/T = 0.063$, we simulated with a seed of $f(0) = 0$ (solid line) and $f(0) \approx 1475$ ($\psi = 0.075 a_s^{-3/2}$) (dashed line). Error bands are obtained from the variance of ten independent runs.

$\mu/T = 0.063$. The error bands indicate the variance over ten independent runs and thus illustrate the demand for statistics in the zero mode. The long-time zero-mode occupancy appears to converge for all chemical potentials and especially the two simulations with different seed for $\mu/T = 0.063$ are consistent with each other within the error bands. All runs used in the remainder of this chapter have been performed without a seed in the zero-mode. The full spectra $f(k) \equiv \langle f(k, \vartheta) \rangle_{\vartheta_0}^{\vartheta_{\max}}$ for three of the five configurations shown in Fig. 11 are depicted in Fig. 12, as obtained from averaging up to $\vartheta_{\max} = 10^4 a_s$. They approach the Bose-Einstein distribution for $\mu = 0$, while Rayleigh-Jeans scaling at low k is not expected to be reached exactly in the finite-volume case.

2. Shift of the critical temperature

Let us now turn to the determination of the shift of the transition temperature due to interactions. At leading order in the dimensionless interaction strength, set by the diluteness η, Eq. (10), the shift scales as $\eta^{2/3}$ [60], and to next-to-leading order in η, it takes the form [61]

$$\frac{\Delta T_c}{T_c^0} = c\eta^{2/3} + [c'\ln(\eta^{2/3}) + c'']\eta^{4/3}, \qquad (32)$$

where c, c', and c'' are numerical constants, $T_c^0 = [\rho/\zeta(3/2)]^{2/3} 2\pi/m$ is the critical temperature of the ideal Bose gas in $d = 3$ dimensions and $\Delta T_c \equiv T_c - T_c^0$ is the shift of its value in the presence of interactions.

While, in principle, a thorough determination of the transition point requires carefully extrapolating to the infinite-
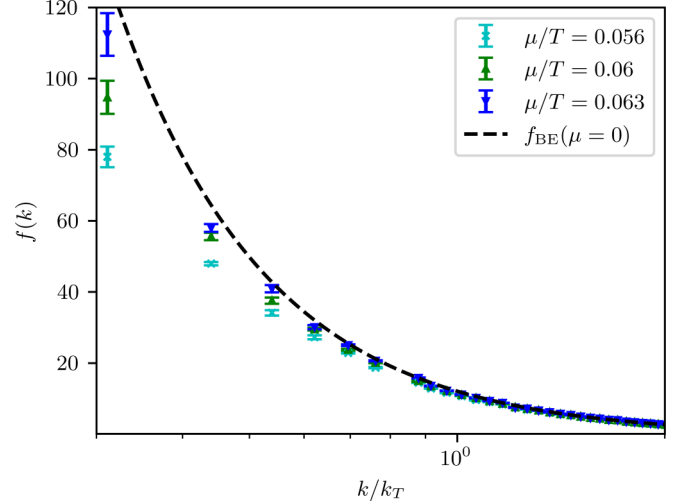

FIG. 12. Infrared part of the momentum spectrum of the interacting single-component gas for three different chemical potentials μ close to and below the transition obtained by averaging up to $\vartheta_{\max} = 10^4 a_s$. All other parameters are as in Fig. 11. Note that here only the k axis carries a log scale for better visibility.

volume limit, for the case of a weakly interacting gas we can employ a somewhat simpler approach. Consider the condensate fraction ρ_0/ρ in a free gas as a function of T/T_c^0, for a fixed temperature T, and system size $\mathcal{V} = L^3$, and thus fixed ratio $\ell = L/\lambda_T$ of the system size L and the thermal wavelength $\lambda_T = \sqrt{2\pi/mT}$. Varying the chemical potential μ allows tuning the total density $\rho = N/\mathcal{V}$ as well as the zero-mode density $\rho_0 = f(0)/\mathcal{V}$, and the critical temperature T_c^0, such that

$$T/T_c^0 = \ell^2 \left(\frac{\zeta(3/2)}{N}\right)^{2/3}, \qquad (33)$$

$$\rho_0/\rho = \frac{z}{1-z} N^{-1}, \qquad (34)$$

where $z = \exp(\beta\mu)$ is the fugacity. The total particle number as a function of z in the continuum limit can be determined as the sum

$$N = \sum_{m_x m_y m_z} \frac{1}{z^{-1} \exp\left[\pi \ell^{-2}\left(m_x^2 + m_y^2 + m_z^2\right)\right] - 1}, \qquad (35)$$

where the sums are performed over $m_i = -M_i, \ldots, M_i$, with $M_x = M_y = M_z$ chosen large enough to ensure convergence. The resulting dependence of the ideal-gas condensate fraction ρ_0/ρ on T/T_c^0 is shown in Fig. 13 as a solid cyan line. For comparison, the inset shows the same curve over a wider range near the critical temperature, together with the critical scaling $\rho_0/\rho = 1 - (T/T_c^0)^{3/2}$ (black solid line), which results in the thermodynamic limit $\mathcal{V} \to \infty$.

For the weakly interacting Bose gas, we make use of the approximation, that the functional form of the condensate fraction as a function of T in units of the critical temperature is the same as in the noninteracting case, albeit with a shifted critical temperature, i.e.,

$$[\rho_0/\rho](T/T_c^0) = [\rho_0/\rho]_{\text{free}}(\alpha T/T_c^0), \qquad (36)$$
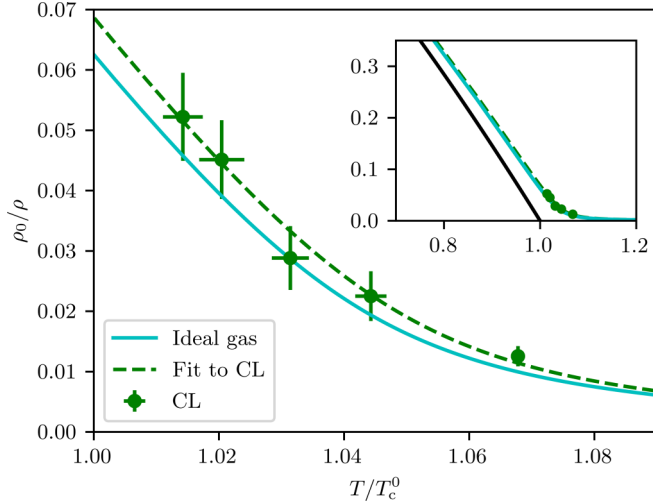
FIG. 13. Condensate fraction ρ_0/ρ as a function of T/T_c^0, for a fixed temperature $T = 1.25a_s^{-1}$, coupling $g = 0.5a_s^2$ and system size $(64a_s)^3$. The values obtained from the CL simulation for the five different chemical potentials μ from Fig. 11 (green data points) are compared with the behavior of the ideal Bose gas (cyan solid line). The dashed green line represents a fit of the ideal-gas behavior, with shifted critical temperature, to the simulation data as described in the main text, which gives $c = 0.58 \pm 0.16$ quantifying the interaction-induced shift (32). The inset depicts the same curves and data together with the near-critical condensate fraction in the thermodynamic limit (black solid line).

with $\alpha = T_c^0/T_c$ and thus $\Delta T_c/T_c^0 = 1/\alpha - 1$. Within errors, this is confirmed by our data. For each of the chemical potentials chosen in our CL simulations, we determine the total density ρ from the sum over the occupation number spectrum over all points of the momentum-time lattice, which we correct by the difference between the continuum and lattice densities determined for the ideal gas at the same temperature and chemical potential, see Appendix B 4 for details. In this way, we determine condensate fractions and corresponding values of T/T_c^0 for the five different near-critical $\mu \in \{0.063, \ldots, 0.056\}$ considered above, which we can compare, cf. Fig. 13, with the behavior of the ideal gas in the continuum.

A least-squares fit of the ideal-gas curve to the simulation data (dashed green line) yields an interaction-induced shift of the critical temperature of

$$\Delta T_c/T_c^0 = 1/\alpha - 1 = 0.004\,97 \pm 0.001\,38. \qquad (37)$$

Possible finite-size corrections to this result are discussed in Appendix D. For the density at $\mu/T = 0.063$ the diluteness becomes $\eta = 7.95 \times 10^{-4}$. As a consequence, neglecting the $O(\eta^{4/3})$ corrections in Eq. (32), the constant c in Eq. (32) takes the value

$$c = 0.58 \pm 0.16. \qquad (38)$$

The determination of the constant c has a long and controversial history [62–69], see Ref. [70] for a review. Within the errors, our result (38) is in good agreement with the value $c = 0.7$ (no error provided) from Ref. [64], while it is larger than $c = 0.34 \pm 0.03$ from the PIMC simulations of Ref. [63] and smaller than the average of more recent results which accumu-

late near $c \approx 1.3$, compare $c = 1.32 \pm 0.02$ from Ref. [67], $c = 1.29 \pm 0.05$ from Ref. [71] [Monte Carlo simulation of classical $O(2)$ field theory], $c = 1.27 \pm 0.11$ from Ref. [68] (variational perturbation theory), and $c = 1.32 \pm 0.14$ from Ref. [69] (PIMC simulation). Experiments with helium in Vycor glasses have found $c \approx 5.1$ [65], while this has been disputed in Ref. [66].

We also note that in Ref. [61] the constants c' and c'', which quantify the corrections to (32) of order $\eta^{4/3}$ were determined. The authors found $c = 1.32 \pm 0.02$, $c' = 19.7518$, and $c'' = 75.7 \pm 0.4$, which for our diluteness $\eta = 7.95 \times 10^{-4}$ yield an $O(\eta^{4/3})$ correction to the shift $[c'\ln(\eta^{2/3}) + c'']\eta^{4/3} = -0.001\,35 \pm 0.000\,03$ and a total shift of $\Delta T_c/T_c^0 = 0.009\,98 \pm 0.000\,17$, which is to be compared with (37). To distinguish numerically the leading-order and next-to-leading-order contributions would require an analysis for a range of different densities or interaction strengths and thus dilutenesses, which is beyond the scope of the present work.

In summary, our analysis demonstrates that the CL method gives access to a beyond mean-field quantity (in the mean-field approximation, there is no shift of the transition temperature), consistent with previous results by order of magnitude.

IV. CONCLUSION AND OUTLOOK

We have shown that it is possible to evaluate the coherent-state path integral of the interacting Bose gas from first principles by means of the complex Langevin (CL) method in experimentally relevant coupling regimes. We found that the spectra and dispersions obtained via the Hartree-Fock and Bogoliubov approximations are well reproduced above and below the transition, respectively. By determining the shift of the critical temperature ΔT_c due to interactions, we could show that the method is in principle capable of providing corrections beyond mean-field approximations. This opens a perspective on possibilities of using CL for *ab initio* simulations of interacting Bose gases in a wide range of experimental settings.

A remaining potential challenge is using the method in the regime of strong-coupling strengths. Here we find CL to perform very well in the experimentally relevant regime of dilute gases, with diluteness parameter $\eta \approx 10^{-3}$, without the need for additional improvements such as adaptive time-step size or regulators. Notwithstanding this, choosing a diluteness of one order of magnitude higher ($\eta \approx 10^{-2}$, corresponding to a by two orders higher particle density), we encounter runaways into the complex plane of field values, which are typical for the method in parameter regimes, in which the so-called sign problem prevails. While such highly dense Bose gases are experimentally difficult to realize, it remains an interesting task beyond the scope of our work to determine the limits up to which the CL method leads to meaningful results in an efficient manner.

For dilute systems, the method promises to be useful in many different contexts, e.g., trapped systems beyond the local density approximation [72], two-dimensional gases near the Berezinskii-Kosterlitz-Thouless transition [73,74], or spinor gases beyond the U($\mathcal{N}$)-symmetric case [4], for

exploring the phase diagram in comparison with mean-field predictions [75,76], or the exploration of anomalous averages and their interplay with the gaplessness of the spectrum [77]. In principle, one may consider CL also for simulating real-time path integrals and thus time evolving systems. This, however, poses a far more challenging sign problem, so far providing access to short-time evolution only [78].

APPENDIX A: DISCRETE LANGEVIN EQUATIONS

In this Appendix, we provide details of the discretization of the action (8) and the complex Langevin equations (5) derived from it.

We express the complex Bose fields in terms of its real and imaginary parts as

$$\psi_a \equiv \varphi_a + i\chi_a. \tag{A1}$$

Discretizing these components on the $N_s^3 \times N_\tau$ lattice, $\varphi_a(\tau, \mathbf{x}) = \varphi_a(ia_\tau, \mathbf{j}a_s) \equiv \varphi_{a,i,\mathbf{j}}$, etc. for χ_a, the action (8) can be written as

$$
\begin{aligned}
S^{\text{lat}} = a_s^3 a_\tau \sum_{i,\mathbf{j}} \Bigg\{ &\sum_a \Bigg[\frac{\varphi_{a,i,\mathbf{j}} - \varphi_{a,i-1,\mathbf{j}}}{a_\tau} \varphi_{a,i,\mathbf{j}} + \frac{\chi_{a,i,\mathbf{j}} - \chi_{a,i-1,\mathbf{j}}}{a_\tau} \chi_{a,i,\mathbf{j}} + i\frac{\varphi_{a,i-1,\mathbf{j}}\chi_{a,i,\mathbf{j}} - \varphi_{a,i,\mathbf{j}}\chi_{a,i-1,\mathbf{j}}}{a_\tau} \\
&- \frac{1}{2ma_s^2}(\varphi_{a,i+1,\mathbf{j}}\Delta^{\text{lat}}\varphi_{a,i,\mathbf{j}} + \chi_{a,i+1,\mathbf{j}}\Delta^{\text{lat}}\chi_{a,i,\mathbf{j}} + i\varphi_{a,i+1,\mathbf{j}}\Delta^{\text{lat}}\chi_{a,i,\mathbf{j}} - i\chi_{a,i+1,\mathbf{j}}\Delta^{\text{lat}}\varphi_{a,i,\mathbf{j}}) \\
&- \mu(\varphi_{a,i+1,\mathbf{j}}\varphi_{a,i,\mathbf{j}} + \chi_{a,i+1,\mathbf{j}}\chi_{a,i,\mathbf{j}} + i\varphi_{a,i+1,\mathbf{j}}\chi_{a,i,\mathbf{j}} - i\varphi_{a,i,\mathbf{j}}\chi_{a,i+1,\mathbf{j}}) \Bigg] \\
&+ \frac{g}{2}\Bigg(\sum_a \{\varphi_{a,i+1,\mathbf{j}}\varphi_{a,i,\mathbf{j}} + \chi_{a,i+1,\mathbf{j}}\chi_{a,i,\mathbf{j}} + i\varphi_{a,i+1,\mathbf{j}}\chi_{a,i,\mathbf{j}} - i\varphi_{a,i,\mathbf{j}}\chi_{a,i+1,\mathbf{j}}\} \Bigg)^2 \Bigg\},
\end{aligned}
\tag{A2}
$$

where the index i enumerates the imaginary time lattice sites with spacing a_τ, the three-dimensional index vector $\mathbf{j}$ the spatial lattice sites, with discretization a_s. Δ^{lat} is the Laplacian on the lattice, i.e.,

$$\Delta^{\text{lat}}A_{a,i,\mathbf{j}} \equiv A_{a,i,\mathbf{j}+\mathbf{e}_x} + A_{a,i,\mathbf{j}-\mathbf{e}_x} + A_{a,i,\mathbf{j}+\mathbf{e}_y} + A_{a,i,\mathbf{j}-\mathbf{e}_y} + A_{a,i,\mathbf{j}+\mathbf{e}_z} + A_{a,i,\mathbf{j}-\mathbf{e}_z} - 6A_{a,i,\mathbf{j}}, \tag{A3}$$

with $\mathbf{e}_{x,y,z}$ being the unit vectors in three dimensions. Note that ψ_a^* must be evaluated infinitesimally later than ψ_a, i.e., at lattice point $i + 1$ rather than at i, as can be seen from the construction of the coherent-state path integral where in each time step ψ_a^* is evaluated with respect to the coherent state on the left while ψ_a acts to the right, on the state one step earlier. This is important even in the analytical treatment where it ensures the right convergence in the complex Matsubara plane [79].

The corresponding Langevin equations are obtained from (A2) by taking derivatives with respect to φ and χ,

$$
\begin{aligned}
\frac{\partial \varphi_{a,i,\mathbf{j}}}{\partial \vartheta} = &a_s^3(\varphi_{a,i+1,\mathbf{j}} + \varphi_{a,i-1,\mathbf{j}} - 2\varphi_{a,i,\mathbf{j}} + i\chi_{a,i-1,\mathbf{j}} - i\chi_{a,i+1,\mathbf{j}}) + \frac{a_s a_\tau}{2m}\Delta^{\text{lat}}(\varphi_{a,i-1,\mathbf{j}} + \varphi_{a,i+1,\mathbf{j}} + i\chi_{a,i-1,\mathbf{j}} - i\chi_{a,i+1,\mathbf{j}}) \\
&+ \mu a_s^3 a_\tau(\varphi_{a,i-1,\mathbf{j}} + \varphi_{a,i+1,\mathbf{j}} + i\chi_{a,i-1,\mathbf{j}} - i\chi_{a,i+1,\mathbf{j}}) \\
&- g a_s^3 a_\tau(\Psi_{i-1,\mathbf{j}}\varphi_{a,i-1,\mathbf{j}} + \Psi_{i,\mathbf{j}}\varphi_{a,i+1,\mathbf{j}} + i\Psi_{i-1,\mathbf{j}}\chi_{a,i-1,\mathbf{j}} - i\Psi_{i,j,k,l}\chi_{a,i+1,\mathbf{j}}) + \eta(\vartheta)
\end{aligned}
\tag{A4}
$$

and

$$
\begin{aligned}
\frac{\partial \chi_{a,i,\mathbf{j}}}{\partial \vartheta} = &a_s^3(\chi_{a,i+1,\mathbf{j}} + \chi_{a,i-1,\mathbf{j}} - 2\chi_{a,i,\mathbf{j}} - i\varphi_{a,i-1,\mathbf{j}} + i\varphi_{a,i+1,\mathbf{j}}) + \frac{a_s a_\tau}{2m}\Delta^{\text{lat}}(\chi_{a,i-1,\mathbf{j}} + \chi_{a,i+1,\mathbf{j}} - i\varphi_{a,i-1,\mathbf{j}} + i\varphi_{a,i+1,\mathbf{j}}) \\
&+ \mu a_s^3 a_\tau(\chi_{a,i-1,\mathbf{j}} + \chi_{a,i+1,\mathbf{j}} - i\varphi_{a,i-1,\mathbf{j}} + i\varphi_{a,i+1,\mathbf{j}}) - g a_s^3 a_\tau(\Psi_{i-1,\mathbf{j}}\chi_{a,i-1,\mathbf{j}} \\
&+ \Psi_{i,\mathbf{j}}\chi_{a,i+1,\mathbf{j}} - i\Psi_{i-1,\mathbf{j}}\varphi_{a,i-1,\mathbf{j}} + i\Psi_{i,\mathbf{j}}\varphi_{a,i+1,\mathbf{j}}) + \eta(\vartheta),
\end{aligned}
\tag{A5}
$$

where

$$\Psi_{i,\mathbf{j}} \equiv \sum_a (\varphi_{a,i+1,\mathbf{j}}\varphi_{a,i,\mathbf{j}} + \chi_{a,i+1,\mathbf{j}}\chi_{a,i,\mathbf{j}} + i\varphi_{a,i+1,\mathbf{j}}\chi_{a,i,\mathbf{j}} - i\varphi_{a,i,\mathbf{j}}\chi_{a,i+1,\mathbf{j}}). \tag{A6}$$

Note that both φ and χ must now be taken to be *complex* variables, such that the complex Langevin method requires to evolve *four* real fields per component instead of two as in classical GPE simulations.

APPENDIX B: NUMERICAL EXTRACTION OF THE OBSERVABLES

1. Spectrum and dispersion on the lattice

The translation of the occupation number $\langle a_{\mathbf{k}}^\dagger a_{\mathbf{k}} \rangle$ to the lattice gives $\langle \psi_{\mathbf{k},i+1}^* \psi_{\mathbf{k},i} \rangle$, where, as for the action, ψ^* must be evaluated at the temporal lattice point $i+1$ and ψ at i, following from the construction of the coherent-state path integral, cf. Appendix A. When computing the dispersion, more care is in order. In the operator formalism, we can write it as

$$\omega(\mathbf{k}) = \sqrt{-\frac{\partial_\tau \partial_{\tau'} \langle a_{\mathbf{k}}^\dagger(\tau) a_{\mathbf{k}}(\tau') \rangle|_{\tau=\tau'}}{\langle a_{\mathbf{k}}^\dagger(\tau) a_{\mathbf{k}}(\tau') \rangle|_{\tau=\tau'}}}. \tag{B1}$$

The discretization of $\partial_\tau \partial_{\tau'} \langle a_{\mathbf{k}}^\dagger(\tau) a_{\mathbf{k}}(\tau') \rangle|_{\tau=\tau'}$ on the temporal lattice is somewhat subtle. Since $\langle a_{\mathbf{k}}^\dagger(\tau) a_{\mathbf{k}}(\tau') \rangle|_{\tau=\tau'}$ translates to $\langle \psi_{\mathbf{k},i+1}^* \psi_{\mathbf{k},i} \rangle$, one is tempted to naively write $\langle (\psi_{\mathbf{k},i+2}^* - \psi_{\mathbf{k},i+1}^*)(\psi_{\mathbf{k},i+1} - \psi_{\mathbf{k},i}) \rangle/a_\tau^2$. This, however, does *not* correspond to the operator finite-time differences:

$$\langle [a_{\mathbf{k}}^\dagger(\tau + a_\tau) - a_{\mathbf{k}}^\dagger(\tau)][a_{\mathbf{k}}(\tau + a_\tau) - a_{\mathbf{k}}(\tau)] \rangle/a_\tau^2, \tag{B2}$$

which contain an anti-time-ordered term, and thus cannot be simply translated to $\langle (\psi_{\mathbf{k},i+2}^* - \psi_{\mathbf{k},i+1}^*)(\psi_{\mathbf{k},i+1} - \psi_{\mathbf{k},i}) \rangle/a_\tau^2$.

Hence, a better choice is to discretize the product of derivatives as

$$\begin{aligned}
\partial_\tau \partial_{\tau'} \langle a_{\mathbf{k}}^\dagger(\tau) a_{\mathbf{k}}(\tau') \rangle|_{\tau=\tau'} \approx \langle [a_{\mathbf{k}}^\dagger(\tau + a_\tau) - a_{\mathbf{k}}^\dagger(\tau)] \\
\times [a_{\mathbf{k}}(\tau) - a_{\mathbf{k}}(\tau - a_\tau)] \rangle/a_\tau^2,
\end{aligned} \tag{B3}$$

which contains time-ordered terms only and implies the discretization

$$\omega(\mathbf{k}) = \sqrt{-\frac{\langle [\psi_{\mathbf{k},i+2}^* - \psi_{\mathbf{k},i+1}^*][\psi_{\mathbf{k},i} - \psi_{\mathbf{k},i-1}] \rangle}{a_\tau^2 \langle \psi_{\mathbf{k},i+1}^* \psi_{\mathbf{k},i} \rangle}} \tag{B4}$$

of the dispersion, which we finally sum over i, in which is it homogeneous, to gain statistics.

2. Momentum and integrals over momentum

On a lattice of size $L = N_x a_s = N_y a_s = N_z a_s \equiv N_s a_s$, the kinetic energy associated with the momentum mode with indices (j_x, j_y, j_z) is not given by $E_{\text{kin}} = (2\pi/L)^2(j_x^2 + j_y^2 + j_z^2)/2m$ as in the continuum. The discretization (A3) of the Laplacian rather implies the energy to be sine-spaced, i.e.,

$$E_{\text{kin}} = \frac{2}{ma_s^2}\left[\sin^2\left(\frac{\pi j_x}{N_x}\right) + \sin^2\left(\frac{\pi j_y}{N_y}\right) + \sin^2\left(\frac{\pi j_z}{N_z}\right)\right]. \tag{B5}$$

Accordingly, the modulus k of the momentum associated with mode (j_x, j_y, j_z) reads

$$k = \frac{2}{a_s}\sqrt{\sin^2\left(\frac{\pi j_x}{N_x}\right) + \sin^2\left(\frac{\pi j_y}{N_y}\right) + \sin^2\left(\frac{\pi j_z}{N_z}\right)}. \tag{B6}$$

In computing $f(k)$ and $\omega(k)$ we perform angular averages and accumulate the momenta into bins of width $(64a_s)^{-1}$. For the eight lowest bins, which contain only a single value of k, we use this value as the k coordinate in plots of functions of momentum, while for all other bins we choose the center of the bin.

Integrals over momentum space such as necessary for determining the mean density ρ are evaluated as sums as

$$\rho = \frac{1}{L^3} \sum_{j_x j_y j_z} \left|\cos\left(\frac{\pi j_x}{N_x}\right)\cos\left(\frac{\pi j_y}{N_y}\right)\cos\left(\frac{\pi j_z}{N_z}\right)\right| f_{j_x j_y j_z}, \tag{B7}$$

where we choose again $N_{x,y,z} \equiv N_s = L/a_s$ such that the sums run over $j_{x,y,z} = 0, \dots, N_s - 1$, and where $f_{j_x j_y j_z} = \langle \psi_{\mathbf{j},i+1}^* \psi_{\mathbf{j},i} \rangle$ is the occupation number of mode $\mathbf{j} = (j_x, j_y, j_z)$, averaged over imaginary time, cf. (12), i.e., summed over i, cf. Appendix B 3. The factor in Eq. (B7) containing cosines is a Jacobian that takes into account the sine-spacing of the lattice momenta.

3. Truncated Matsubara expansion of particle spectrum and dispersion

For the purpose of numerical simulations, the imaginary time interval $[0, \beta]$ must be discretized. Here we want to discuss in more detail the errors induced by this discretization. Consider, e.g., the expectation value $f(\mathbf{k}, \tau) = \langle a_{\mathbf{k}}^\dagger(\tau) a_{\mathbf{k}}(\tau) \rangle$ of the particle number operator in mode $\mathbf{k}$, for a single-component gas.

In the continuum, dropping any momentum indices, the expectation value can be written as

$$f = \langle a^\dagger a \rangle = \frac{\text{Tr}\{e^{-\beta\omega a^\dagger a} a^\dagger a\}}{\text{Tr}\{e^{-\beta\omega a^\dagger a}\}}. \tag{B8}$$

Evaluating this expression in the number-state basis gives the Bose-Einstein distribution,

$$\langle a^\dagger a \rangle = \frac{1}{e^{\beta\omega} - 1}. \tag{B9}$$

Within the path integral formulation, the thermal expectation value of the number operator is represented by an imaginary-time path integral, the discretized Feynman representation of which reads

$$\langle a^\dagger a \rangle = \lim_{N_\tau \to \infty} \frac{1}{N_\tau} \sum_j \frac{\int \prod_i d\psi_i^* d\psi_i e^{-S_{N_\tau}[\boldsymbol{\psi}]} \psi_{j+1}^* \psi_j}{\int \prod_i d\psi_i^* d\psi_i e^{-S_{N_\tau}[\boldsymbol{\psi}]}}, \tag{B10}$$

with the time-discretized action ($a_\tau = \beta/N_\tau$)

$$S_{N_\tau}[\boldsymbol{\psi}] = \sum_{i=0}^{N_\tau - 1}(\psi_i^* \psi_i - \psi_{i+1}^* \psi_i + a_\tau \omega \psi_{i+1}^* \psi_i), \tag{B11}$$

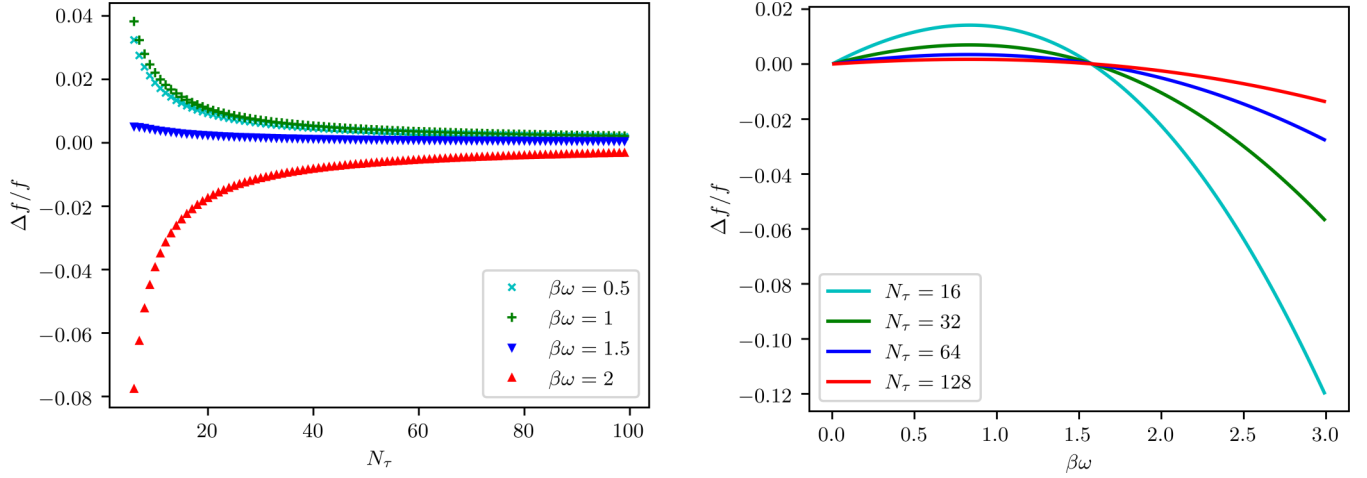where the index N_τ is identified with the index 0.

FIG. 14. Relative error $\Delta f / f = [f(N_\tau) - f]/f$ of the particle number $f(N_\tau)$, Eq. (B15), with respect to the continuum value f, Eq. (B8), (left panel) for different values of $\beta\omega$ in dependence of the truncation order N_τ and (right panel) for different truncation orders N_τ as function of $\beta\omega$, with N_τ increasing from the (on the left side) uppermost curve to the lowermost one.

Expanding the fields on the finite time interval $[0, \beta]$ in terms of Matsubara modes,

$$\psi_j = \frac{1}{\sqrt{\beta}} \sum_{n=0}^{N_\tau - 1} \tilde{\psi}_n e^{i\omega_n j a_\tau}, \quad (B12)$$

with the Matsubara frequencies $\omega_n = 2\pi n/\beta$, $n = 0, \ldots, N_\tau - 1$, the path integral (B10) becomes

$$\langle a^\dagger a \rangle = \lim_{N_\tau \to \infty} \frac{1}{\beta} \sum_{m=0}^{N_\tau - 1} \frac{\int \prod_n d\tilde{\psi}_n^* d\tilde{\psi}_n e^{-S_{N_\tau}[\tilde{\psi}]} \tilde{\psi}_m^* \tilde{\psi}_m e^{-i\omega_m a_\tau}}{\int \prod_n d\tilde{\psi}_n^* d\tilde{\psi}_n e^{-S_{N_\tau}[\tilde{\psi}]}}, \quad (B13)$$

with

$$S_{N_\tau}[\tilde{\psi}] = \sum_{n=0}^{N_\tau - 1} \left(\frac{1 - e^{-i\omega_n a_\tau}}{a_\tau} + \omega e^{-i\omega_n a_\tau} \right) \tilde{\psi}_n^* \tilde{\psi}_n. \quad (B14)$$

Performing the Gaussian integrals yields

$$\langle a^\dagger a \rangle = \lim_{N_\tau \to \infty} \frac{1}{\beta} \sum_n \frac{e^{-i\omega_n a_\tau}}{a_\tau^{-1}(1 - e^{-i\omega_n a_\tau}) + \omega e^{-i\omega_n a_\tau}}$$

$$= \lim_{N_\tau \to \infty} \sum_n \frac{1}{N_\tau(e^{2\pi i n/N_\tau} - 1) + \beta\omega}$$

$$\equiv \lim_{N_\tau \to \infty} f(N_\tau). \quad (B15)$$

One shows in a similarly way that the dispersion ω, defined in Eq. (B4), for finite N_τ becomes

$$\omega(N_\tau) = \frac{N_\tau}{\beta} \sqrt{-\frac{1}{f(N_\tau)} \sum_n \frac{2e^{-2\pi i n/N_\tau} - e^{-4\pi i n/N_\tau} - 1}{N_\tau(e^{2\pi i n/N_\tau} - 1) + \beta\omega}}. \quad (B16)$$

In the continuum limit, $N_\tau \to \infty$, the series (B15) converges to $1/(e^{\beta\omega} - 1)$. On the lattice, however, the series needs to be truncated at some finite N_τ, such that an error occurs which depends on N_τ, but also on the value of $\beta\omega$. Figure 14 shows the numerically computed truncation error for several combinations of N_τ and $\beta\omega$. In the right panel, one sees that the relative

error for small $\beta\omega$ is positive but turns negative at some point and quickly becomes rather large (while the absolute error still decreases). This illustrates the needs in temporal resolution for a precise evaluation of small occupation numbers as well as of the corresponding dispersions, the limits of which can be seen in Figs. 1–8. In fact, for large enough $\beta\omega$, the relative error on the particle number can even become -100%, as can be seen from Fig. 15, which shows a version of Fig. 1 including the part of the spectrum up to $k_{\max} = 2\sqrt{3} a_s^{-1}$.

4. Finite-resolution corrections near criticality

On the computational lattice, systematic deviations of observables from their continuum counterparts are caused by both the finite number of Matsubara modes and the finite spatial lattice resolution. Both mainly affect the UV properties of the system and therefore, in describing the critical behavior near the phase transition, are expected to give a small correc-
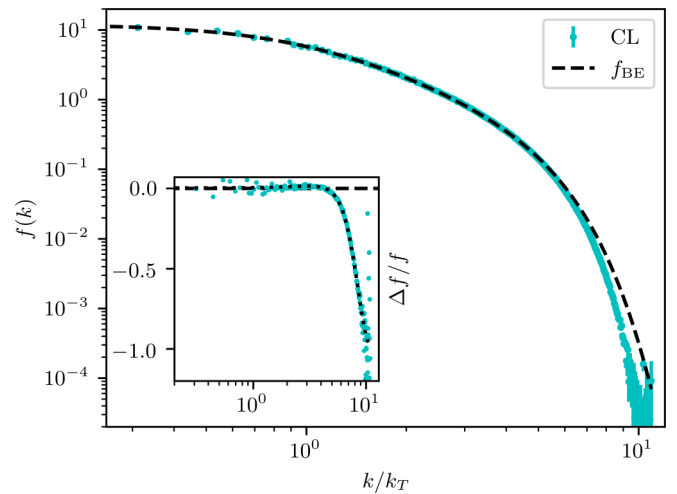

FIG. 15. The same angle-averaged momentum spectrum as shown in Fig. 1, but including the highest momenta in the "corners" of the momentum lattice, i.e., up to $k_{\max} = 2\sqrt{3} a_s^{-1}$.

tion only. Furthermore, for a weakly interacting gas above the transition, the spectrum is well approximated by an ideal-gas Bose-Einstein distribution with a shifted chemical potential, see Sec. III E. It is thus reasonable to account for the described systematic errors in the following way: For a free gas at $\mu \to 0$ in a box of fixed size $\mathcal{V} = L^3$, we numerically determine the deviation $\delta\rho = \rho(N_s \to \infty, N_\tau \to \infty) - \rho(N_s, N_\tau)$ between the density on the lattice and in the continuum (but for finite system size $\mathcal{V}$). $\delta\rho$ is then added to the density determined from numerical data for the interacting system. For the parameters as chosen in Sec. III G, i.e., a $64^3 \times 16$ lattice at $T = 1.25 a_s^{-1}$, we obtain $\delta\rho = 0.00154 a_s^{-3}$. This is a

rather small correction, but it is significant in determining the constant c.

APPENDIX C: BOGOLIUBOV THEORY OF U($\mathcal{N}$) SYMMETRIC BOSE GAS

In this Appendix, we provide, for conciseness, some details on the Bogoliubov mean-field description of an $\mathcal{N}$-component Bose gas described by the U($\mathcal{N}$) symmetric Hamiltonian (9). For a complete discussion in the context of spinor Bose gases, see, e.g., Refs. [4,76]. In momentum space, the "Kamiltonian" entering the grand-canonical ensemble reads

$$\hat{K} \equiv \hat{H} - \mu\hat{N} = \sum_{\mathbf{k}} \sum_{\alpha} \left(\frac{\mathbf{k}^2}{2m} - \mu\right) a_{\mathbf{k},\alpha}^\dagger a_{\mathbf{k},\alpha} + \frac{g}{2\mathcal{V}} \sum_{\mathbf{k}\mathbf{k}'\mathbf{q}} \sum_{\alpha\alpha'} a_{\mathbf{k}+\mathbf{q},\alpha}^\dagger a_{\mathbf{k}'-\mathbf{q},\alpha'}^\dagger a_{\mathbf{k},\alpha} a_{\mathbf{k}',\alpha'}, \tag{C1}$$

where $\alpha, \alpha' = 1, \ldots, \mathcal{N}$ enumerate the different field components, g is the coupling, and $\mathcal{V}$ is the volume. Making the Bogoliubov ansatz $a_{\mathbf{k},\alpha} = \sqrt{\mathcal{V}\rho_0}\delta_{\mathbf{k}0} + a_{\mathbf{k},\alpha}(1 - \delta_{\mathbf{k}0})$ and expanding to quadratic order in the nonzero mode operator, this becomes

$$\hat{K} = \left(\frac{\mathcal{N}g}{2}\rho_0 - \mu\right)\mathcal{N}\mathcal{V}\rho_0 + \sum_{\mathbf{k}\neq0} \sum_{\alpha} \left(\frac{\mathbf{k}^2}{2m} + \mathcal{N}g\rho_0 - \mu\right) a_{\mathbf{k},\alpha}^\dagger a_{\mathbf{k},\alpha}$$

$$+ g\rho_0 \sum_{\mathbf{k}\neq0} \sum_{\alpha\alpha'} \left[a_{\mathbf{k},\alpha}^\dagger a_{\mathbf{k},\alpha'} + \frac{1}{2}(a_{\mathbf{k},\alpha} a_{-\mathbf{k},\alpha'} + a_{\mathbf{k},\alpha}^\dagger a_{-\mathbf{k},\alpha'}^\dagger)\right] + O(a_{\mathbf{k},\alpha}^3), \tag{C2}$$

where ρ_0 is the condensate density, which is chosen equal in each component, such that the total condensate density is $\mathcal{N}\rho_0$. To diagonalize in the component degree of freedom, we introduce

$$B_{\mathbf{k}} = \frac{1}{\sqrt{\mathcal{N}}} \sum_{\alpha} a_{\mathbf{k},\alpha}, \tag{C3}$$

$$b_{\mathbf{k},\beta} = \sum_{\alpha} w_\beta^\alpha a_{\mathbf{k},\alpha}, \quad \beta = 1, \ldots, \mathcal{N} - 1, \tag{C4}$$

where the vectors $\mathbf{w}_\beta$ form an arbitrary orthonormal basis of the $\mathcal{N} - 1$ dimensional orthogonal complement of the $\mathcal{N}$-component vector $(1, 1, \ldots, 1)^T / \sqrt{\mathcal{N}}$. Thereby we obtain

$$\hat{K} = \left(\frac{\mathcal{N}g}{2}\rho_0 - \mu\right)\mathcal{N}\mathcal{V}\rho_0 + \sum_{\mathbf{k}\neq0} \left(\frac{\mathbf{k}^2}{2m} + 2\mathcal{N}g\rho_0 - \mu\right) B_{\mathbf{k}}^\dagger B_{\mathbf{k}} + \frac{\mathcal{N}g\rho_0}{2} \sum_{\mathbf{k}\neq0} (B_{\mathbf{k}} B_{-\mathbf{k}} + B_{\mathbf{k}}^\dagger B_{-\mathbf{k}}^\dagger)$$

$$+ \sum_{\mathbf{k}\neq0} \sum_{\beta} \left(\frac{\mathbf{k}^2}{2m} + \mathcal{N}g\rho_0 - \mu\right) b_{\mathbf{k},\beta}^\dagger b_{\mathbf{k},\beta} + O(a_{\mathbf{k},\alpha}^3). \tag{C5}$$

The equivalence of (C2) and (C5) can be easily seen by plugging the transformation (C3) and (C4) into (C5) and exploiting the fact that $(1, 1, \ldots, 1)^T / \sqrt{\mathcal{N}}$ and the $\mathbf{w}_\beta$ form an orthonormal set. In leading-order mean-field approximation the energy is minimized at the chemical potential $\mu = \mathcal{N}g\rho_0$. Upon inserting this, (C5) becomes

$$\hat{K} = -\frac{g}{2}\mathcal{N}^2\rho_0^2\mathcal{V} + \sum_{\mathbf{k}\neq0} \left(\frac{\mathbf{k}^2}{2m} + \mathcal{N}g\rho_0\right) B_{\mathbf{k}}^\dagger B_{\mathbf{k}} + \frac{\mathcal{N}g\rho_0}{2} \sum_{\mathbf{k}\neq0} (B_{\mathbf{k}} B_{-\mathbf{k}} + B_{\mathbf{k}}^\dagger B_{-\mathbf{k}}^\dagger) + \sum_{\mathbf{k}\neq0} \sum_{\beta} \frac{\mathbf{k}^2}{2m} b_{\mathbf{k},\beta}^\dagger b_{\mathbf{k},\beta} + O(a_{\mathbf{k},\alpha}^3), \tag{C6}$$

which describes Bogoliubov modes $B_{\mathbf{k}}$ and $\mathcal{N} - 1$ free Goldstone excitations $b_{\mathbf{k},\beta}$. The total occupation number $f(\mathbf{k}) = \sum_a \langle|\psi_a(\mathbf{k})|^2\rangle$ for $\mathbf{k} \neq 0$ can then be written as

$$f(\mathbf{k}) = \sum_{\alpha} a_{\mathbf{k},\alpha}^\dagger a_{\mathbf{k},\alpha} = B_{\mathbf{k}}^\dagger B_{\mathbf{k}} + \sum_{\beta} b_{\mathbf{k},\beta}^\dagger b_{\mathbf{k},\beta} = \frac{1}{2}\left[\frac{\varepsilon(\mathbf{k}) + \mathcal{N}g\rho_0}{\omega(\mathbf{k})} - 1\right] + \frac{\varepsilon(\mathbf{k}) + \mathcal{N}g\rho_0}{\omega(\mathbf{k})(e^{\beta\omega(\mathbf{k})} - 1)} + \frac{\mathcal{N} - 1}{e^{\beta\varepsilon(\mathbf{k})} - 1}, \tag{C7}$$

with Bogoliubov and free dispersions

$$\omega(\mathbf{k}) = \sqrt{\varepsilon(\mathbf{k})(\varepsilon(\mathbf{k}) + 2\mathcal{N}g\rho_0)}, \tag{C8}$$

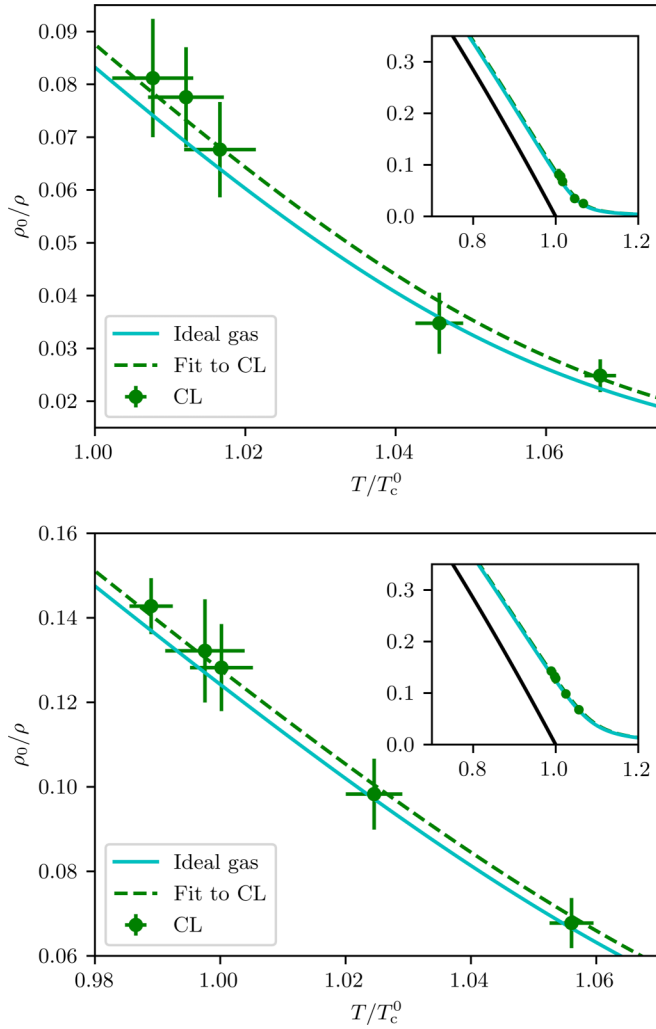$$\varepsilon(\mathbf{k}) = \frac{\mathbf{k}^2}{2m}. \tag{C9}$$

FIG. 16. The same as in Fig. 13, but on a 48^3 (upper panel) and 32^3 (lower panel) lattice.

APPENDIX D: POSSIBLE FINITE-SIZE EFFECTS IN EXTRACTION OF ΔT_c

In our extraction of the transition temperature shift due to interaction effects we refrained from performing a systematic finite-size analysis. Numerical results by Ref. [71] (who performed such a systematic analysis and defined the shift in the finite system in a manner similar to ours) suggest that for the system size that was employed here (20.2 thermal wavelengths λ_T), finite-size corrections are already significantly smaller than our statistical error. Namely, they find the shift of the critical temperature to scale with system size L as

$$\frac{\Delta T_c}{T_c^0} \sim \frac{1}{1 + b_0 g(2m)^{3/2} T^{1/2} + \frac{a_1 + b_1 g(2m)^{3/2} T^{1/2}}{(Lm^2 Tg)^{1.038}}}, \quad \text{(D1)}$$

with $a_1 = 1.29$, $b_0 = 0.123$, $b_1 = 0.744$.[2] For our parameters and system size, we obtain from this formula a deviation of 14.6% between the finite-L and the $L \to \infty$ value for the shift, which is only half our statistical error (27.8%), which justifies our procedure.

Our own simulations corroborate said weak dependence on L. To demonstrate this, we perform the same analysis as in the main text but for the smaller 48^3 and 32^3 lattices, for the exact same chemical potentials. The result is shown in Fig. 16. Here we obtain for the shift

$$\Delta T_c/T_c^0 = 0.0036 \pm 0.0014 \ (48^3 \text{lattice}), \quad \text{(D2)}$$

$$\Delta T_c/T_c^0 = 0.0031 \pm 0.0008 \ (32^3 \text{lattice}). \quad \text{(D3)}$$

Within the errors, this agrees with the result for the 64^3 lattice, suggesting that finite-size effects already play a minor role.

------

[2]Note that, in Ref. [71], constants were chosen $2m = T = 1$ in the factors multiplying b_0 and b_1.

[1] L. Pitaevskii and S. Stringari, *Bose-Einstein Condensation and Superfluidity* (Oxford University Press, Oxford, 2016).

[2] S. Giorgini, L. P. Pitaevskii, and S. Stringari, Phys. Rev. A **54**, R4633 (1996).

[3] D. Hutchinson and P. Blakie, Int. J. Mod. Phys. B **20**, 5224 (2006).

[4] D. M. Stamper-Kurn and M. Ueda, Rev. Mod. Phys. **85**, 1191 (2013).

[5] P. Henelius and A. W. Sandvik, Phys. Rev. B **62**, 1102 (2000).

[6] M. Lombardo, Mod. Phys. Lett. A **22**, 457 (2007).

[7] M. G. Alford and A. Kryjevski, J. Phys. G **37**, 025002 (2010).

[8] G. Aarts, Phys. Rev. Lett. **102**, 131601 (2009).

[9] S. Pilati, K. Sakkos, J. Boronat, J. Casulleras, and S. Giorgini, Phys. Rev. A **74**, 043621 (2006).

[10] G. Spada, S. Pilati, and S. Giorgini, Phys. Rev. A **105**, 013325 (2022).

[11] A. Sinatra, C. Lobo, and Y. Castin, J. Phys. B: At., Mol. Opt. Phys. **35**, 3599 (2002).

[12] P. B. Blakie, A. S. Bradley, M. J. Davis, R. J. Ballagh, and C. W. Gardiner, Adv. Phys. **57**, 363 (2008).

[13] M. J. Davis, S. A. Morgan, and K. Burnett, Phys. Rev. Lett. **87**, 160402 (2001).

[14] M. J. Davis, S. A. Morgan, and K. Burnett, Phys. Rev. A **66**, 053618 (2002).

[15] M. Boninsegni, N. V. Prokof'ev, and B. V. Svistunov, Phys. Rev. E **74**, 036701 (2006).

[16] K. Van Houcke, E. Kozik, N. Prokof'ev, and B. Svistunov, Phys. Procedia **6**, 95 (2010).

[17] Z. Fodor, S. D. Katz, and C. Schmidt, J. High Energy Phys. (online) 03 (2007) 121.

[18] C. Gattringer and K. Langfeld, Int. J. Mod. Phys. A **31**, 1643007 (2016).

[19] M. G. Endres, Phys. Rev. D **75**, 065012 (2007).

[20] H. J. M. van Bemmel, D. F. B. ten Haaf, W. van Saarloos, J. M. J. van Leeuwen, and G. An, Phys. Rev. Lett. **72**, 2442 (1994).

[21] W. M. C. Foulkes, L. Mitas, R. J. Needs, and G. Rajagopal, Rev. Mod. Phys. **73**, 33 (2001).

[22] S. M. Rothstein, E. Ospadov, and C. Bruzzese, in *Mathematical Physics in Theoretical Chemistry*, edited by S. M. Blinder and J. E. House (Elsevier, Amsterdam, 2019), pp. 189–217.

[23] M. Cristoforetti, F. Di Renzo, and L. Scorzato (Aurora Science Collaboration), Phys. Rev. D **86**, 074506 (2012).

[24] J. M. Pawlowski, M. Scherzer, C. Schmidt, F. P. G. Ziegler, and F. Ziesché, Phys. Rev. D **103**, 094505 (2021).

[25] G. Parisi, Phys. Lett. B **131**, 393 (1983).

[26] J. R. Klauder and W. P. Petersen, J. Stat. Phys. **39**, 53 (1985).

[27] E. Seiler, EPJ Web Conf. **175**, 01019 (2018).

[28] A. Gilchrist, C. W. Gardiner, and P. D. Drummond, Phys. Rev. A **55**, 3014 (1997).

[29] P. Deuar and P. D. Drummond, J. Phys. A: Math. Gen. **39**, 1163 (2006).

[30] P. Deuar and P. D. Drummond, J. Phys. A: Math. Gen. **39**, 2723 (2006).

[31] G. Aarts and I.-O. Stamatescu, J. High Energy Phys. (online) 09 (2008) 018.

[32] D. Sexty, Phys. Lett. B **729**, 108 (2014).

[33] J. B. Kogut and D. K. Sinclair, Phys. Rev. D **100**, 054512 (2019).

[34] Y. Ito, H. Matsufuru, Y. Namekawa, J. Nishimura, S. Shimasaki, A. Tsuchiya, and S. Tsutsui, J. High Energy Phys. (online) 10 (2020) 144.

[35] A. C. Loheac and J. E. Drut, Phys. Rev. D **95**, 094502 (2017).

[36] L. Rammelmüller, A. C. Loheac, J. E. Drut, and J. Braun, Phys. Rev. Lett. **121**, 173001 (2018).

[37] T. Hayata and A. Yamamoto, Phys. Rev. A **92**, 043628 (2015).

[38] F. Attanasio and J. E. Drut, Phys. Rev. A **101**, 033617 (2020).

[39] C. E. Berger, L. Rammelmüller, A. C. Loheac, F. Ehmann, J. Braun, and J. E. Drut, Phys. Rep. **892**, 1 (2021).

[40] L. Kades, M. Gärttner, T. Gasenzer, and J. M. Pawlowski, Phys. Rev. E **105**, 045315 (2022).

[41] G. Aarts, E. Seiler, and I.-O. Stamatescu, Phys. Rev. D **81**, 054508 (2010).

[42] T. Hayata, Y. Hidaka, and Y. Tanizaki, Nucl. Phys. B **911**, 94 (2016).

[43] J. Nishimura and S. Shimasaki, Phys. Rev. D **92**, 011501(R) (2015).

[44] G. Aarts and F. A. James, PoS (**LATTICE2010**), 321 (2010).

[45] E. Seiler, D. Sexty, and I.-O. Stamatescu, Phys. Lett. B **723**, 213 (2013).

[46] F. Attanasio and B. Jäger, Eur. Phys. J. C **79**, 1 (2019).

[47] D. Alvestad, R. Larsen, and A. Rothkopf, J. High Energy Phys. 08 (2021) 138.

[48] H. Gausterer and S. Lee, J. Stat. Phys. **73**, 147 (1993).

[49] K. Nagata, J. Nishimura, and S. Shimasaki, Phys. Rev. D **94**, 114515 (2016).

[50] L. L. Salcedo, Phys. Rev. D **94**, 114505 (2016).

[51] M. Scherzer, E. Seiler, D. Sexty, and I.-O. Stamatescu, Phys. Rev. D **99**, 014512 (2019).

[52] M. Scherzer, E. Seiler, D. Sexty, and I.-O. Stamatescu, Phys. Rev. D **101**, 014501 (2020).

[53] H. Stoof and M. Bijlsma, J. Low Temp. Phys. **124**, 431 (2001).

[54] C. W. Gardiner, J. R. Anglin, and T. I. A. Fudge, J. Phys. B: At., Mol. Opt. Phys. **35**, 1555 (2002).

[55] C. W. Gardiner and M. J. Davis, J. Phys. B: At., Mol. Opt. Phys. **36**, 4731 (2003).

[56] S. Cockburn and N. Proukakis, Laser Phys. **19**, 558 (2009).

[57] S. Gautam, A. Roy, and S. Mukerjee, Phys. Rev. A **89**, 013612 (2014).

[58] A. Polkovnikov, Ann. Phys. (NY) **325**, 1790 (2010).

[59] F. Dalfovo, S. Giorgini, L. P. Pitaevskii, and S. Stringari, Rev. Mod. Phys. **71**, 463 (1999).

[60] G. Baym, J.-P. Blaizot, M. Holzmann, F. Laloë, and D. Vautherin, Phys. Rev. Lett. **83**, 1703 (1999).

[61] P. Arnold, G. Moore, and B. Tomášik, Phys. Rev. A **65**, 013606 (2001).

[62] H. Stoof, Phys. Rev. A **45**, 8398 (1992).

[63] P. Grüter, D. Ceperley, and F. Laloë, Phys. Rev. Lett. **79**, 3549 (1997).

[64] M. Holzmann, P. Grüter, and F. Laloë, Eur. Phys. J. B **10**, 739 (1999).

[65] J. D. Reppy, B. C. Crooker, B. Hebral, A. D. Corwin, J. He, and G. M. Zassenhaus, Phys. Rev. Lett. **84**, 2060 (2000).

[66] P. Arnold and B. Tomášik, Phys. Rev. A **62**, 063604 (2000).

[67] P. Arnold and G. Moore, Phys. Rev. Lett. **87**, 120401 (2001).

[68] B. Kastening, Phys. Rev. A **69**, 043613 (2004).

[69] K. Nho and D. P. Landau, Phys. Rev. A **70**, 053614 (2004).

[70] J. O. Andersen, Rev. Mod. Phys. **76**, 599 (2004).

[71] V. A. Kashurnikov, N. V. Prokof'ev, and B. V. Svistunov, Phys. Rev. Lett. **87**, 120402 (2001).

[72] V. V. Goldman, I. F. Silvera, and A. J. Leggett, Phys. Rev. B **24**, 2870 (1981).

[73] C. J. Foster, P. B. Blakie, and M. J. Davis, Phys. Rev. A **81**, 023623 (2010).

[74] N. Prokof'ev, O. Ruebenacker, and B. Svistunov, Phys. Rev. Lett. **87**, 270402 (2001).

[75] Y. Kawaguchi, N. T. Phuc, and P. B. Blakie, Phys. Rev. A **85**, 053611 (2012).

[76] Y. Kawaguchi and M. Ueda, Phys. Rep. **520**, 253 (2012).

[77] V. I. Yukalov and H. Kleinert, Phys. Rev. A **73**, 063612 (2006).

[78] J. Berges, S. Borsanyi, D. Sexty, and I.-O. Stamatescu, Phys. Rev. D **75**, 045007 (2007).

[79] A. Altland and B. D. Simons, *Condensed Matter Field Theory*, 2nd ed. (Cambridge University Press, Cambridge, 2010).